CHEMISTRY OF MATERIALS

Article

Self-Assembly of Two-Dimensional Bimetallic Nickel-Cobalt Phosphate Nanoplates into One-Dimensional Porous Chain-Like Architecture for Efficient Oxygen Evolution Reaction

Ni Luh Wulan Septiani, Yusuf Valentino Kaneti, Kresna Bondan Fathoni, Kenya Kani, Abeer Enaiet Allah, Brian Yuliarto, * Nugraha, Hermawan Kresno Dipojono, Zeid A Alothman, Dmitri Golberg, and Yusuke Yamauchi

Chem. Mater., **Just Accepted Manuscript** • DOI: 10.1021/acs.chemmater.0c02385 • Publication Date (Web): 17 Jul 2020

Just Accepted

is published by the American Chemical Society. 1155 Sixteenth Street N.W., Washington, DC 20036

Self-Assembly of Two-Dimensional Bimetallic Nickel-Cobalt Phosphate Nanoplates into One-Dimensional Porous Chain-Like Architecture for Efficient Oxygen Evolution Reaction

Ni Luh Wulan Septiani[1], Yusuf Valentino Kaneti[2]*, Kresna Bondan Fathoni[1], Kenya Kani[3], Abeer Enaiet Allah[4], Brian Yuliarto[1,5]*, Nugraha[1,5], Hermawan Kresno Dipojono[1,5], Zeid A. Alothman,[6] Dmitri Golberg[2,7,8]* and Yusuke Yamauchi[3,9]*

1 *Department of Engineering Physics, Institute of Technology Bandung (ITB), Bandung 40132, Indonesia*

2 *International Center for Materials Nanoarchitectonics (WPI-MANA), National Institute for Materials Science (NIMS), 1-1 Namiki, Tsukuba, Ibaraki 305-0044, Japan*

3 *School of Chemical Engineering and Australian Institute for Bioengineering and Nanotechnology (AIBN), The University of Queensland, Brisbane, QLD 4072, Australia*

4 *Department of Chemistry, Faculty of Science, Beni-Suef University, Beni-Suef 62511, Egypt*

5 *Research Center for Nanosciences and Nanotechnology (RCNN), Institute of Technology Bandung (ITB), Bandung 40132, Indonesia*

6 *Chemistry Department, College of Science, King Saud University, Riyadh 11451, Saudi Arabia*

7 *Centre for Materials Science, Queensland University of Technology, 2 George str., Brisbane, QLD 4000, Australia*

8 *School of Chemistry and Physics, Science and Engineering Faculty, Queensland University of Technology, 2 George str., Brisbane, QLD 4000, Australia*

9 *Department of Plant and Environmental New Resources, Kyung Hee University, 1732 Deogyeong-daero, Giheung-gu, Yongin-si, Gyeonggi-do, 446-701, South Korea*

E-mails: KANETI.Valentino@nims.go.jp; brian@tf.itb.ac.id; y.yamauchi@uq.edu.au; dmitry.golberg@qut.edu.au

Abstract

The self-assembly of two-dimensional (2D) nanostructures into one-dimensional (1D) nanoarchitectures may result in materials which combine the unique physicochemical properties of 2D nanostructures with the excellent charge transport properties of 1D architectures. Herein, we report, the self-stacking of 2D nickel-cobalt (Ni-Co) phosphate nanoplates into 1D chain-like architectures with the assistance of metal glycerates as self-templates. This unique self-assembly process is driven by the adsorbed ethyl glycerate on the surface of the individual nanoplates, which promotes the subsequent growth of the new nanoplate on top of the previously formed nanoplate, thereby leading to the self-stacking of these nanoplates along the vertical direction. The flexibility of the proposed method is also highlighted by the feasible preparation of nickel phosphate with the same self-assembled structure. When tested as a catalyst for oxygen evolution reaction (OER) in an alkaline medium, the bimetallic Ni-Co phosphate (derived from Ni-Co-TEP) with the nanoplate-assembled chain-like structure displays much lower overpotential (η_{10}= 310 mV) and Tafel slope (74 mV dec^{-1}) than its pristine counterparts. The enhanced OER activity of this bimetallic catalyst may be attributed to: (i) the highly interconnected structure and the bimetallic composition which promote improved charge transport; (ii) the porous chain-like structure which provides increased number of active sites and facilitates; (iii) the presence of Ni^{3+} and Co^{3+} active sites (nickel-cobalt (oxy)hydroxides) which can promote the chemisorption of OH^- and facilitate electron transfer from the OH^- to the surface Ni/Co sites during OER.

1. Introduction

Achieving the precise control over the orientation and spatial arrangement of nanomaterials is highly desirable to promote good interconnectivity between nanoparticles, generate anisotropic properties, and achieve superior functional performance. The self-assembly of nanoparticles can be achieved either through naturally-driven interactions (*e.g.*, depletion attraction, capillary forces, dipole-dipole interactions) or with the assistance of external templates or surface modifications.[1] These external templates typically include polymers, patterned matrix, and large molecules. Recently, two-dimensional (2D) nanomaterials have been intensively researched owing to their high-surface-area to volume ratios, unique physicochemical properties, and good mechanical stability. As a consequence, they have been widely employed in the fields of energy storage and conversion, sensing, and optoelectronics. The self-organization of 2D nanostructures (*e.g.*, nanosheets, nanoplates, nanoflakes) into hierarchical 3D structures (*e.g.*, flower-like, urchin-like, star-like, *etc*.) has been frequently observed in various inorganic materials, such as metal oxides,[2-3] phosphates,[4-5] sulfides,[6-7] phosphides,[8-9] and hydroxides,[10-11]. In addition, the self-assembly of 0D nanostructures, such as nanocrystals or nanoparticles into one-dimensional (1D) nanoarchitectures, such as supertubes and superlattice chains, has previously been achieved by solvent-induced association of clusters and confined assembly, respectively.[12-13] In contrast, the self-assembly of 2D nanostructures into 1D architecture is rarely reported due to the difficulty in confining the growth of 2D nanostructures in one particular direction. Such self-assembled structures may not only inherit the uniqueness of 2D nanostructures but also the excellent charge transport of 1D nanomaterials. However, to date, such self-assembly process has been largely limited to common 2D layered materials, such as graphene oxide and metal dichalcogenides (*e.g.*, molybdenum disulfide (MoS_2), tantalum disulfide (TaS_2), and tungsten diselenide (WSe_2).[14]

Electrocatalytic water splitting provides a green and sustainable approach for generating clean hydrogen energy. Water electrolysis involves two major reactions, namely oxygen evolution reaction (OER) and hydrogen evolution reaction. The OER process suffers from sluggish kinetics involving multi-step proton-coupled electron transfer, which leads to high overpotentials. To accelerate this process, state-of-the-art catalysts based on iridium oxide (IrO_2) or ruthenium oxide (RuO_2) are usually employed. However, the scarcity and high cost of these catalysts have motivated scientists to search for alternative low-cost

electrocatalysts for OER based on non-precious metals, such as metal hydroxides,[15-17] metal oxides,[18-20] metal sulfides,[21-23] metal phosphides,[24-26] metal phosphates,[27-29] and so on. Among them, transition metal phosphates have attracted increasing attention for water splitting reactions due to their layered structures, high electrochemical activities, open frameworks with large channels/cavities, and wide variations in valence states. Previously, various metal phosphate nanostructures have been investigated for electrocatalytic OER. For instance, 1D cobalt pyrophosphate (CoP_2O_7) nanowires and nanobelts exhibited overpotentials (η_{10}) of 359 and 371 mV to reach a current density of 10 mA cm^{-2} and Tafel slopes of 54.1 and 57.9 mV dec^{-1}, respectively.[30] In comparison, 2D CoP_2O_7 nanoleaves and nanorhombuses displayed higher overpotentials of 390 and 424 mV and Tafel slopes of 81.6 and 119 mV dec^{-1}, respectively. Nanosheet-assembled flower-like zinc-cobalt phosphate catalyst exhibited an overpotential of 382 mV and a Tafel slope of 83.2 mV dec^{-1}.[29] The nanosheet-assembled flower-like structures contributed to the increase of active sites and improved the electron transfer. Similarly, 3D flower-like bimetallic cobalt-based phosphide catalysts assembled of ultrathin nanosheets (CoM-P-3DHFLMs) exhibited enhanced OER activities with low overpotentials ranging from 292 to 318 mV, owing to their sheet-assembled 3D hierarchical structures.[8] These previous studies highlight the benefits of self-assembled nanoarchitectures for enhancing the OER performance of metal phosphate-based catalysts. However, to the best of our knowledge, the self-assembly of 2D metal phosphate nanostructures into 1D architectures has rarely been reported.

In this work, we report the self-assembly of uniform Ni-Co phosphate nanoplates into porous 1D chain-like particles through the solvothermal reaction of uniform Ni-Co glycerate particles with triethyl phosphate (TEP) at 180 °C, followed by annealing in air at 600 °C. Here, the utilization of metal glycerate as the precursor is essential for generating ethyl glycerate during the solvothermal reactions, which is responsible for the self-stacking of these nanoplates into chain-like structures. Interestingly, using the same method, but replacing the Ni-Co glycerate with nickel glycerate and cobalt glycerate, amorphous nickel phosphate chain-like particles (Ni-Co-TEP-600) and holey cobalt pyrophosphate (Co-TEP-600) microplates are obtained, respectively, thus confirming the flexibility of the proposed strategy. The electrocatalytic properties of the bimetallic Ni-Co phosphate sample (Ni-Co-TEP-600) derived from Ni-Co-TEP towards OER were evaluated and compared with its pristine counterparts (Ni-TEP-600 and Co-TEP-600). The electrochemical measurements reveal the

superior catalytic activity of the bimetallic Ni-Co phosphate (Ni-Co-TEP-600) chain-like particles towards OER compared to amorphous nickel phosphate (Ni-TEP-600) chain-like particles and holey cobalt pyrophosphate (Co-TEP-600) microplates, as indicated by their lower overpotential and Tafel slope. Furthermore, this bimetallic phosphate catalyst also exhibits high electrochemical stability for OER with a negligible change in activity after 16 h of cycling. The possible mechanisms behind the enhanced OER activity of this bimetallic phosphate catalyst have also been proposed.

2. Experimental Section

2.1. Chemicals

Nickel(II) nitrate hexahydrate ($Ni(NO_3)_2 \cdot 6H_2O$ (99.5%)), cobalt(II) nitrate hexahydrate ($Co(NO_3)_2 \cdot 6H_2O$) (99.5%), 2-propanol (C_3H_8O, >99.5%), and ethanol (C_2H_6O, 99.5%) were purchased from Wako Reagent Japan. Triethyl phosphate ($(C_2H_5)_3PO_4$) (≥99.8 %) and Nafion was purchased from Sigma-Aldrich Japan. All chemicals were used directly without any further purification.

2.2. Synthesis of metal glycerate templates

The metal glycerate templates, including nickel glycerate, cobalt glycerate, and nickel-cobalt (Ni-Co) glycerate were prepared by solvothermal methods in accordance with our previous reports.[31-33] To prepare the nickel glycerate particles, 0.5 mmol of $Ni(NO_3)_2 \cdot 6H_2O$ was initially dissolved in 40 mL of 2-propanol followed by the addition of 8 mL of glycerol into this solution under vigorous stirring. The final mixture solution was subsequently transferred into a 100 mL Teflon-lined stainless-steel autoclave and reacted at 180 °C for 16 h in an electric oven. The resulting precipitate was filtered by centrifugation, washed several times with ethanol and then dried at 60 °C overnight. Similar synthetic procedures were used to synthesize the cobalt glycerate spheres, except by replacing $Ni(NO_3) \cdot 6H_2O$ with $Co(NO_3) \cdot 6H_2O$. To prepare the Ni-Co glycerate spheres, 0.25 mmol of $Ni(NO_3)_2 \cdot 6H_2O$ and 0.25 mmol of $Co(NO_3)_2 \cdot 6H_2O$ (Ni : Co molar ratio = 1:1) were first mixed together under stirring. The rest of the synthetic procedures were identical to those used for preparing nickel glycerate spheres.

2.3. Template-assisted fabrication of metal-TEP particles (TEP = triethyl glycerate)

Fabrication of nanoplate-assembled chain-like Ni-Co-TEP particles. In a typical procedure, 0.03 g of the nickel-cobalt glycerate powder was first dispersed in 20 mL of ethanol followed by sonication for 10 min until the powder became well-dispersed. In the next step, 800 μL of triethyl phosphate (TEP) was added dropwise into this suspension under mild stirring. After continuous stirring for 2 h, the final suspension was transferred into a 100 mL Teflon-lined stainless-steel autoclave and solvothermally-reacted in an electric oven at 180 °C for 16 h. The resulting product was collected by centrifugation and washed with ethanol twice, before being dried at 60 °C overnight.

Fabrication of nanoplate-assembled chain-like Ni-TEP particles. The experimental steps for preparing the nanoplate-assembled chain-like Ni-TEP particles were similar to those used for synthesizing Ni-Co-TEP but by replacing the nickel-cobalt glycerate powder with nickel glycerate powder.

Fabrication of holey Co-TEP microplates. The synthetic procedures for preparing the holey Co-TEP microplates were identical to those used for preparing chain-like Ni-TEP particles, except by replacing the nickel glycerate powder with cobalt glycerate powder.

2.4. Conversion of metal-TEP precursors to metal phosphates

The as-prepared Ni-TEP, Co-TEP, and Ni-Co-TEP samples were calcined in air at 600 °C for 2 h at heating rate of 1 °C min^{-1} to obtain porous nickel phosphate, cobalt phosphate, and nickel-cobalt phosphate materials, respectively, which retained the original shapes of the respective metal-TEP precursors. These calcined samples are labeled as Ni-TEP-600, Co-TEP-600, and Ni-Co-TEP-600, respectively.

2.5. Characterization

X-ray diffraction (XRD) patterns of the samples were collected using a Rigaku RINT 2500X diffractometer with Cu Kα radiation (λ= 1.54 Å). The crystallite size was calculated using the Scherrer's equation:

$$D = \frac{K \cdot \lambda}{B \cdot cos\theta} \quad (1)$$

where D is the crystallite size, λ is the X-ray wavelength, β is the width of the peak (full width at half maximum (FWHM)), θ is the Bragg angle and K is the Scherrer constant. Scanning electron microscopy (SEM) imaging was conducted on a Hitachi SU-8000 instrument operated at 5 kV and transmission electron microscopy

(TEM) observation was performed using a JEOL JEM 2100 operated at 200 kV. The elemental contents of the samples were analyzed by ICP-OES (Inductively coupled plasma-optical emission spectrometry) using a Hitachi SPS3520UV-DD instrument. X-ray photoelectron spectroscopy (XPS) measurements were carried out with a ThermoFisher Scientific ESCALAB250Xi with Al Kα radiation. Nitrogen (N_2) adsorption-desorption isotherms were recorded at 77 K using a BELSORP-mini II Sorption System. The surface areas and pore volumes of the products were approximated *via* Brunauer-Emmett-Teller (BET) and Barrett-Joyner-Halenda (BJH) methods, respectively. Prior to the BET analysis, all samples were degassed in vacuum at 150 °C for 16 h to eliminate the adsorbed moisture.

2.6. Electrochemical measurements

Electrochemical measurements of the as-prepared catalysts were conducted using an electrochemical workstation (CHI-660E, CH Instruments, USA) with a three-electrode configuration. Saturated calomel electrode (SCE) and graphite rod were utilized as reference and counter electrodes, respectively and 1.0 M KOH solution was employed as the electrolyte. The working electrode was fabricated by dispersing 4 mg of the catalyst in 950 µL of water. Next, 50 µL of Nafion solution was added into this suspension and the resulting suspension was sonicated for 1 h to produce a homogeneous ink. Then, 5 µL of the catalyst ink (loading= 0.283 mg cm^{-2}) was dropped onto the glassy carbon electrode (GCE) with a standard diameter of 3 mm and dried under ambient atmosphere. Prior to the OER measurements, the KOH electrolyte was bubbled with nitrogen for 0.5 h and the metal phosphate electrodes were stabilized in 1.0 M KOH solution *via* cyclic voltammetry (CV) for 100 cycles until the CV curves become stable. The polarization curves were obtained by linear sweep voltammetry (LSV) measurements at a fixed scan rate of 5 mV s^{-1}. The potential difference between our SCE reference electrode and the standard reversible hydrogen electrode (RHE) (Hydroflex™ Model ET070, USA) was determined to be 0.250 V. Therefore, all measured potentials were converted to RHE by employing the equation:

$$E_{RHE} = E_{SHE} + (0.250 + 0.059 \times pH) \quad (2)$$

The iR compensation was calculated as (potential (V)- internal impendence) x current. The internal impedance takes into account the electrolyte impedance and the electrode impedance. The BET surface area-normalized current density (j_{BET}) was calculated by employing the equation[34]:

$$j_{\mathrm{BET}} = \frac{\boldsymbol{I}}{\mathbf{10} \cdot \boldsymbol{S_{BET}} \cdot \boldsymbol{m}} \quad (3)$$

where I is the current (mA), S_{BET} is the BET surface area ($m^2\ g^{-1}$), and m is the mass loading (0.283 mg cm^{-2}). The overpotential (η) was determined according to the formula:

$$\eta\ (\mathrm{V}) = E\ (\mathrm{RHE}) - 1.23\ \mathrm{V} \quad (4)$$

Tafel plots were derived from the LSV curves, and the Tafel slope was calculated using the equation:

$$\eta = a + b \log j \quad (5)$$

where η, a, b, and j refer to the overpotential, exchange current density, Tafel slope, and current density, respectively. The Nyquist plots were obtained by electrochemical impedance spectroscopy (EIS) measurements in the frequency range of 1-100,000 Hz at a potential of 1.4 V *versus* RHE with an amplitude of 5 mV. The stability of the optimum catalyst (Ni-Co-TEP-600) was assessed by chronoamperometry measurement at a constant overpotential of 310 mV for 16 h in 1.0 M KOH solution using a three-electrode system.

3. Results and discussion

3.1. Morphology, composition, and formation mechanism

XRD patterns of the metal glycerate precursors show a sharp peak at 12° and a shoulder peak at around 36° which are the characteristic peaks of metal glycerates (**Figure S1**). Among the metal glycerate precursors, cobalt glycerate shows the highest degree of crystallinity, while nickel glycerate shows the poorest crystallinity. As expected, the Ni-Co glycerate sample exhibits a moderate degree of crystallinity in between nickel and cobalt glycerates. The morphologies of these three metal glycerate templates are depicted in **Figure 1a-c**. The nickel glycerate precursor is composed of irregular aggregates (**Figure 1a**). In contrast, both cobalt glycerate and nickel-cobalt glycerate particles exhibit uniform spherical morphology with diameters in the range of 400-500 nm (**Figure 1b, c**). These metal glycerate particles serve as sacrificial templates for the formation of metal-TEP products. XRD patterns of the metal-TEP samples clearly indicate the phase transformations of the metal glycerate precursors as a result of the solvothermal reactions with TEP at 180 °C (**Figure 1d**). From **Figure 1d**, it is evident that the Ni-TEP, Co-TEP, and Ni-Co-TEP samples share similar

diffraction patterns. The coordination between Ni/Co and TEP results in two strong peaks at 6.5°,13.1°, 19.7°, 21.1°, and 36.8° which are the characteristic peaks of orthorhombic metal-TEP with layered structures.[35-37]

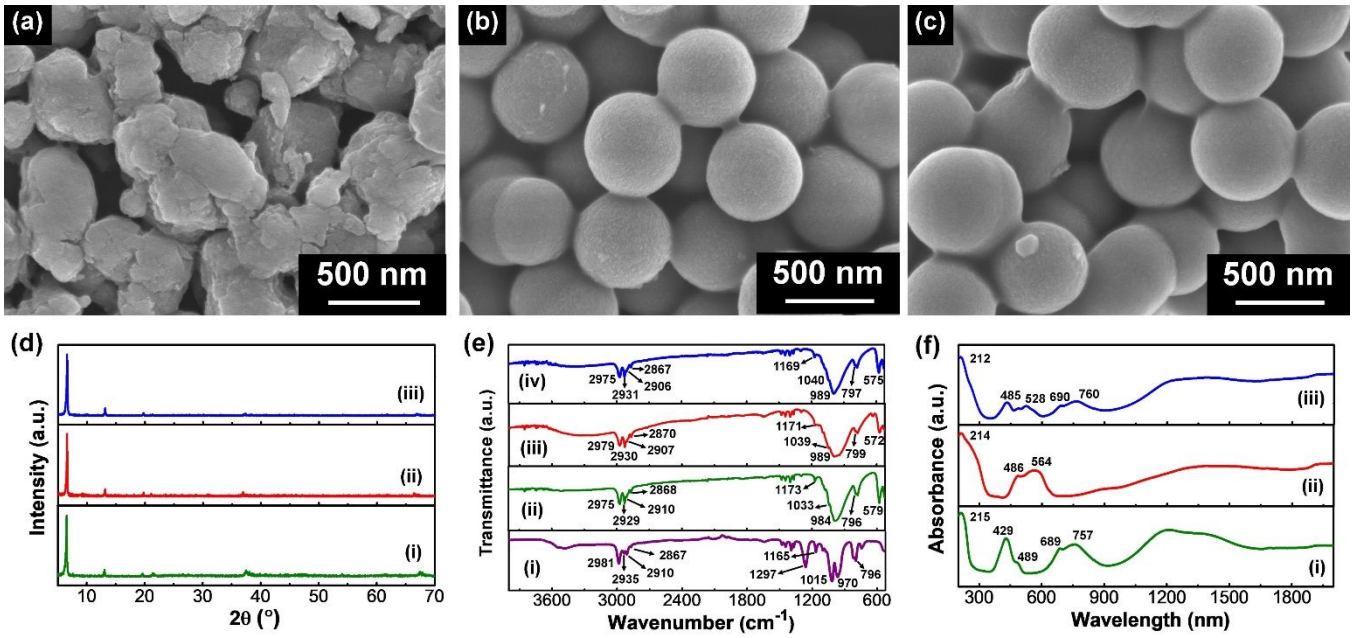

Figure 1. SEM images of (a) nickel glycerate, (b) nickel-cobalt glycerate, and (c) cobalt glycerate particles. (d) XRD patterns of Ni-TEP (i), Ni-Co-TEP (ii), and Co-TEP (iii). (e) FTIR spectra of pure TEP (i), Ni-TEP (ii), Co-TEP (iii), and Ni-Co-TEP (iv). (f) UV-*vis* spectra of Ni-TEP (i), Co-TEP (ii), and Ni-Co-TEP (iii).

To further confirm the formation of metal-TEP, FTIR measurements were carried out. Similar to the XRD results, the FTIR spectra of Ni-TEP, Co-TEP, and Ni-Co-TEP are identical (**Figure 1e**). Furthermore, a comparison of the FTIR spectra of pristine TEP and metal-TEP (*e.g.*, Ni-TEP) reveal some similarities (**Figure S2**). For example, the metal-TEP samples and pure TEP share the symmetric stretching vibrations of C-H in CH_2 and CH_3 modes at around 2867 cm^{-1} and 2910 cm^{-1}, respectively (**Figure 1e**).[38-39] In addition, they both display the IR peaks of asymmetric C-H at around 2930 cm^{-1} and 2978 cm^{-1}. Moreover, metal-TEP and pure TEP share common IR bands between 1365-1485 cm^{-1} indexed to the C-H bending vibration. The IR bands originating from phosphorus compound appear at around 1297 cm^{-1}, and 1171 cm^{-1} in metal-TEP, which are indexed to P=O stretching vibration and P-O-Et rocking vibration, respectively.[40-42] The asymmetric stretching vibration of P-O in pentavalent mode at 970 cm^{-1} in pristine TEP is shifted to a higher wavenumber between 984-989 cm^{-1} in metal-TEP samples, while the symmetric stretching vibration of P-O at 1015 cm^{-1} in pure TEP is shifted to 1042 cm^{-1} in metal-TEP samples. These shifts may be attributed to the interactions between

the metal center and TEP.[43-44] Furthermore, metal-TEP and pristine TEP share a common IR band at ~796 cm^{-1}, which corresponds to the P-O-P stretching vibration. The new IR band appearing at around 772 cm^{-1} in metal-TEP corresponds to the P-O-C stretching vibration. In addition, the disappearance of the P=O band at around 1297 cm^{-1} in metal-TEP samples may be attributed to the interactions between TEP and Ni or Co metal, which causes the breakdown of the P=O bond in TEP (**Figure S2**). The additional peak at around 577 cm^{-1} in metal-TEP samples indicates the bonding between oxygen and metal (Ni or Co), which is not observed in the FTIR spectrum of pristine TEP.[45-48] Using the FTIR spectra of Ni glycerate and Ni-TEP as examples, it is clear that the majority of IR bands belonging to the glycerate compound disappears after the solvothermal reaction (except for some shared bands, such as C-H (1300-1480 cm^{-1}) and metal-oxygen bands (500-600 cm^{-1})), thus suggesting the successful transformation to metal-TEP (**Figure S3**).

UV-*vis* spectroscopy was used to identify the possible formation of metal complexes from the reactions between the metallic constituents in the metal glycerate precursors and TEP during the solvothermal reaction (**Figure 1f**). The UV-*vis* spectrum of Ni-TEP shows strong bands at 429, 489, and 689 nm, along with a broad band at 757 nm (**Figure 1f (i)**). In comparison, the UV-*vis* spectrum of Co-TEP displays broad bands at 479 nm and 564 nm (**Figure 1f (ii)**). These characteristic bands originate from the metal (Ni or Co) to TEP charge transfer transition.[49] As expected, the UV-*vis* spectrum of Ni-Co-TEP shows a combination of the UV-*vis* spectra of Ni-TEP and Co-TEP (**Figure 1f (iii)**). In all three samples, the characteristic band of TEP is observed at around 213 nm, which confirms the formation of metal-TEP complexes. Based on the above XRD, FTIR, and UV-*vis* results, the products obtained from the solvothermal reactions can be confirmed to be metal-TEP.

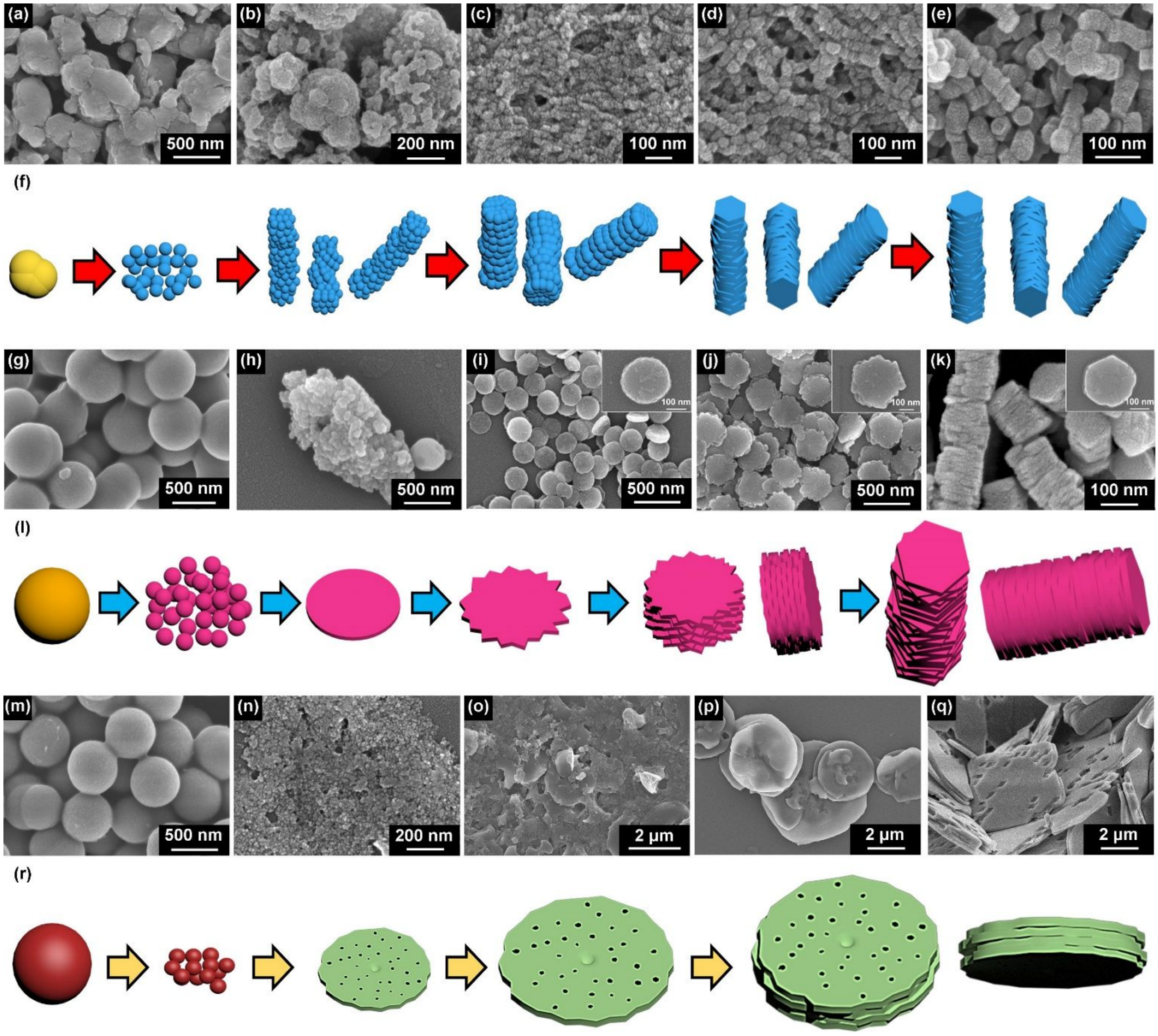

Figure 2. The morphological evolution of the Ni glycerate particles under increasing reaction time with TEP: (a) 0 h, (b) 2 h, (c) 4 h, (d) 8 h, and (e) 16 h. (f) Schematic illustration depicting the formation mechanism of the nanoplate-assembled chain-like Ni-TEP particles from Ni glycerate particles. The morphological transformation of the Ni-Co glycerate particles under increasing reaction time with TEP: (g) 0 h, (h) 2 h, (i) 4 h, (j) 8 h, and (k) 16 h (insets of Figure 2i-k display the high-magnification SEM images of these nanoplates). (l) Schematic diagram showing the formation mechanism of nanoplate-assembled chain-like Ni-Co-TEP particles from Ni-Co glycerate spheres. The shape evolution of the Co glycerate particles under increasing reaction time with TEP: (m) 0 h, (n) 2 h, (o) 4 h, (p) 8 h, and (q) 16 h. (r) Schematic illustration showing the formation mechanism of the holey Co-TEP nanoplates from Co-glycerate spheres.

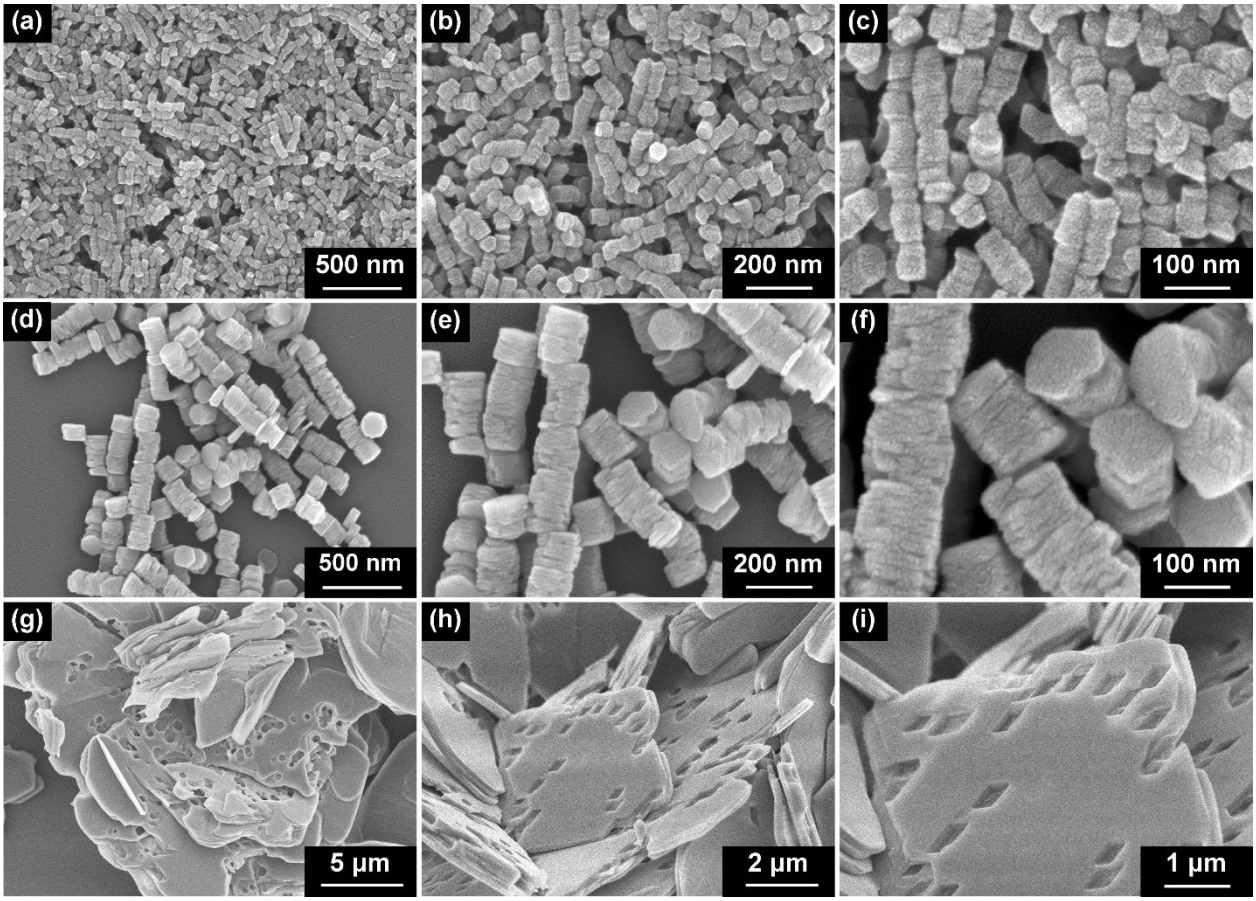

Figure 3. SEM images of (a, b, c) Ni-TEP, (d, e, f) Ni-Co-TEP, and (g, h, i) Co-TEP obtained from the solvothermal reactions of nickel glycerate, cobalt glycerate, and nickel-cobalt glycerate precursors, respectively, with triethyl phosphate (TEP) at 180 ^{o}C for 16 h.

Time-dependent reactions were performed to understand the formation mechanisms of the metal-TEP particles. The morphological evolution of the nickel glycerate precursor with increasing reaction time is depicted in **Figure 2a-e**. The initial nickel glycerate precursor (0 h) consists of irregular aggregates (**Figure 2a**) which become partially deconstructed into smaller nanoparticles after 2 h (**Figure 2b**). After 4 h, the quasi-spherical particles are completely broken down into tiny plate-like particles and start to self-assemble into 1D chain-like particles, however, they are still aggregated to each other (**Figure 2c**). Prolonging the reaction time to 8 h leads to larger aggregated chain-like particles (**Figure 2d**). After 16 h, these chain-like particles become well separated from each other (**Figure 2e**). A schematic illustration depicting the formation mechanism of the nanoplate-assembled chain-like Ni-TEP particles is given in **Figure 2f**. The shape evolution of the Ni-Co glycerate with prolonged reaction time with TEP and the corresponding schematic illustration of the formation

process of Ni-Co-TEP are given in **Figure 2g-k** and **Figure 2l**, respectively. Different from nickel glycerate, the nickel-cobalt glycerate precursor displays a highly uniform spherical morphology with diameters of ~400-500 nm (**Figure 2g**). After 2 h, these spheres are broken into small aggregated particles (**Figure 2h**) which subsequently grow into highly uniform spherical nanoplates with sizes of around 150-200 nm after 4 h (**Figure 2i**). Extending the reaction time to 8 h leads to the transformation of the spherical nanoplates to quasi-hexagonal nanoplates with rough edges, as seen in **Figure 2j**. After 16 h, these nanoplates successfully self-assemble into uniform 1D chain-like particles (**Figure 2k**). The SEM image in the inset of **Figure 2k** reveals the hexagonal morphology of the nanoplate assembling the chain-like Ni-Co-TEP particles.

Similar to Ni-Co glycerate, the cobalt glycerate precursor also possesses a highly uniform spherical morphology (**Figure 2m**). These spherical particles become completely deconstructed into small nanoparticles after 2 h of reaction with TEP (**Figure 2n**). After 4 h, these nanoparticles slowly aggregate together to form some microplates (**Figure 2o**), however the complete transformation into microplates is only achieved after 8 h (**Figure 2p**). These microplates exhibit large diameters in the range of 2-5 μm. Interestingly after 16 h, larger microplates with numerous holes are formed (**Figure 2q**). The sizes of these holes vary from 200 to 250 nm. The morphological evolution of Co-TEP is schematically illustrated in **Figure 2r**. In the early growth stage of Co-TEP, the small particles of cobalt glycerate react with TEP to form large microplates. These quasi-hexagonal microplates are formed from the stacking of smaller plates on top of each other. However, due to the much larger size of Co-TEP, the stacking rate of these plates is significantly slower than those observed in Ni-TEP and Ni-Co-TEP. As a result, the growth rate is uneven among the different plates and the incomplete growth of the smaller plates leaves behind numerous holes on the surface of the large microplates.

Another interesting observation is that in the initial stage (up to 8 h), the growth mechanism of Ni-Co-TEP closely resembles that of Co-TEP. However, beyond this point, the self-stacking behavior of Ni-TEP becomes the more dominant mechanism and the final structure of Ni-Co-TEP follows that of Ni-TEP. Based on the time-dependent experiments, 16 h was selected as the optimum reaction time. SEM images of the optimum Ni-TEP, Co-TEP, and Ni-Co-TEP samples are given in **Figure 3a-i**. From **Figure 3a-f**, it can be seen that both Ni-TEP and Ni-Co-TEP share similar chain-like structures which are formed by the self-stacking of nanoplates along the vertical direction. However, the lengths of the chain-like particles, as well as

the assembling nanoplates are much smaller in the case of Ni-TEP compared to Ni-Co-TEP. In comparison, the Co-TEP product exhibits microplate structure with many visible holes on the surface (**Figure 3g-i**). Some degree of self-stacking of the microplates is observed, however it is far less extensive than those observed in Ni-TEP and Ni-Co-TEP.

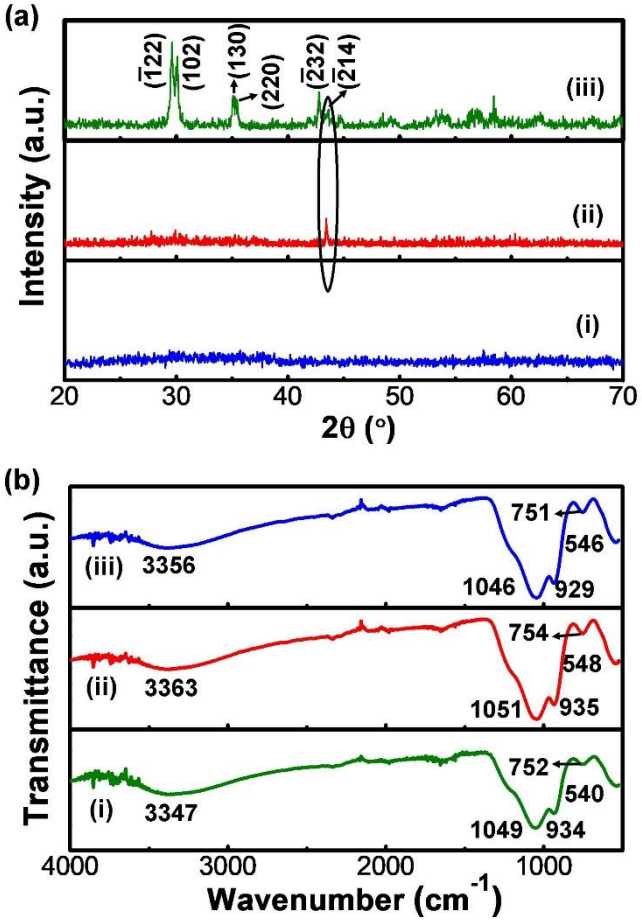

Figure 4. (a) XRD patterns and (b) FTIR spectra of (i) Ni-TEP-600, (ii) Ni-Co-TEP-600, and (iii) Co-TEP-600 after calcination at 600 °C.

The self-assembly of the Ni-Co-TEP nanoplates into chain-like structures is believed to be driven by the unique interactions between glycerate ions and TEP. ICP analysis was carried out to determine the metal to phosphorus (P) ratio, which can help to determine the growth mechanism. Based on the ICP results (**Table S1**), the metal to P ratio is close to 1:1 in all samples, indicating that one metal binds only with one TEP molecule. Therefore, we propose the formation mechanism as follows. In the initial stage, the metal glycerate particles dissociate to form metal ions and glycerate ions. Next, the ethyl group from ethanol reacts with glycerate ions to form ethyl glycerate and releases OH^- as a product. These OH^- ions induce the dissociation

of TEP by releasing one of the ethyl groups followed by the attachment of the OH^- ions onto TEP. At this stage, TEP is converted to diethyl phosphate (DEP), having resonance between the P=O and P-O forms. When DEP, hydroxyl and metal ions react to form metal-DEP, and water is released as a by-product. The FTIR analysis of the supernatant obtained after the solvothermal reaction reveals the presence of ethyl glycerate, as indicated by the presence of three strong peaks between 2975 and 2885 cm^{-1}, indexed to C-H stretching vibrations as well as several narrow, weak peaks in the range of 1454-1248 cm^{-1} attributed to C-H bending vibrations (**Figure S4**).[50-52] Moreover, the change of P=O to P-O is confirmed by the lowering of the intensity of the IR band at 1297 cm^{-1} compared with the P=O band of TEP (**Figure S2**). Based on these results, the overall reaction may be described by the equation:

$$2(Ni/Co)(C_3H_5O_4)_2 + 2P(OC_2H_5)_3O + 2C_2H_5OH \rightarrow Ni_2[P(OC_2H_5)_2O_2]_2O + 4C_3H_5O_4 - C_2H_5 + H_2O \quad (6)$$

It is proposed that the stacking of these nanoplates is driven by the presence of ethyl glycerate which serves as a structure-directing agent. At the later stage of the reaction (*i.e.*, after 8 h), ethyl glycerate becomes sufficiently adsorbed on the surface of the nanoplates and promotes the growth of the new plate on top of the previously formed nanoplate, thereby limiting the lateral growth of the nanoplates. This leads to the self-assembly of the nanoplates in the vertical direction to generate the 1D chain-like architecture. This model is supported by the fact that when the Ni-Co glycerate particles were replaced with nickel and cobalt nitrate salts as the metal precursors to obtain the Ni-Co-TEP, the nanoplate-assembled chain-like morphology was not obtained (**Figure S5**).

The obtained Ni-TEP, Ni-Co-TEP, and Co-TEP precursors were calcined in air at 600 ^oC to obtain the corresponding metal phosphate products. **Figure 4a (i-iii)** displays the XRD patterns of Ni-TEP, Ni-Co-TEP, and Co-TEP samples calcined at 600 °C (the products are denoted as Ni-TEP-600, Ni-Co-TEP-600, and Co-TEP-600). The Ni-TEP-600 sample is completely amorphous as a result of the amorphization of Ni-TEP during heat treatment. This is supported by the TG-DTA analysis, where an endothermic peak is observed at 420 ^oC, followed by another weight loss originating from the decomposition of organic compounds present in the Ni-TEP precursor (**Figure S6a**). Similar to Ni-TEP-600, the bimetallic Ni-Co-TEP-600 sample is also mostly amorphous with a single pronounced peak at around 43.5°. A comparison between **Figure 4a (ii)** and **(iii)** suggests that this single peak may be indexed to the $(\bar{2}14)$ plane of cobalt pyrophosphate (CoP_2O_7). The

average crystallite size of Ni-Co-TEP-600 is measured to be 116 nm according to the Scherrer's formula. The transformation of Ni-Co-TEP into amorphous Ni-Co phosphate seems to take place at ~400 ^{o}C, as indicated by the considerable weight loss in the TG curve of Ni-Co-TEP at this temperature and the exothermic peak in the DTA curve at ~400 °C (**Figure S6b**). The recrystallization of amorphous Ni-Co phosphate occurs at 700 ^{o}C, as indicated by the exothermic peak observed at the same temperature in the DTA curve of Ni-Co-TEP. In contrast, at 600 °C, the Co-TEP precursor is readily transformed into monoclinic cobalt pyrophosphate ($Co_2P_2O_7$), as supported by the presence of major peaks at 29.7°, 30.1°, 35.1°, 35.3°, 42.8°, 43.5, and 58.4°, corresponding to ($\bar{1}22$), (102), (130), (220), ($\bar{2}32$), ($\bar{2}14$), and ($\bar{4}21/\bar{3}34$) planes, respectively (ICSD No. 84-2126-**Table S2**) (**Figure 4a (iii)**). This phase transformation to CoP_2O_7 phase is likely to occur at around 600 °C based on the exothermic peak at the same temperature in the DTA curve (**Figure S6c**).

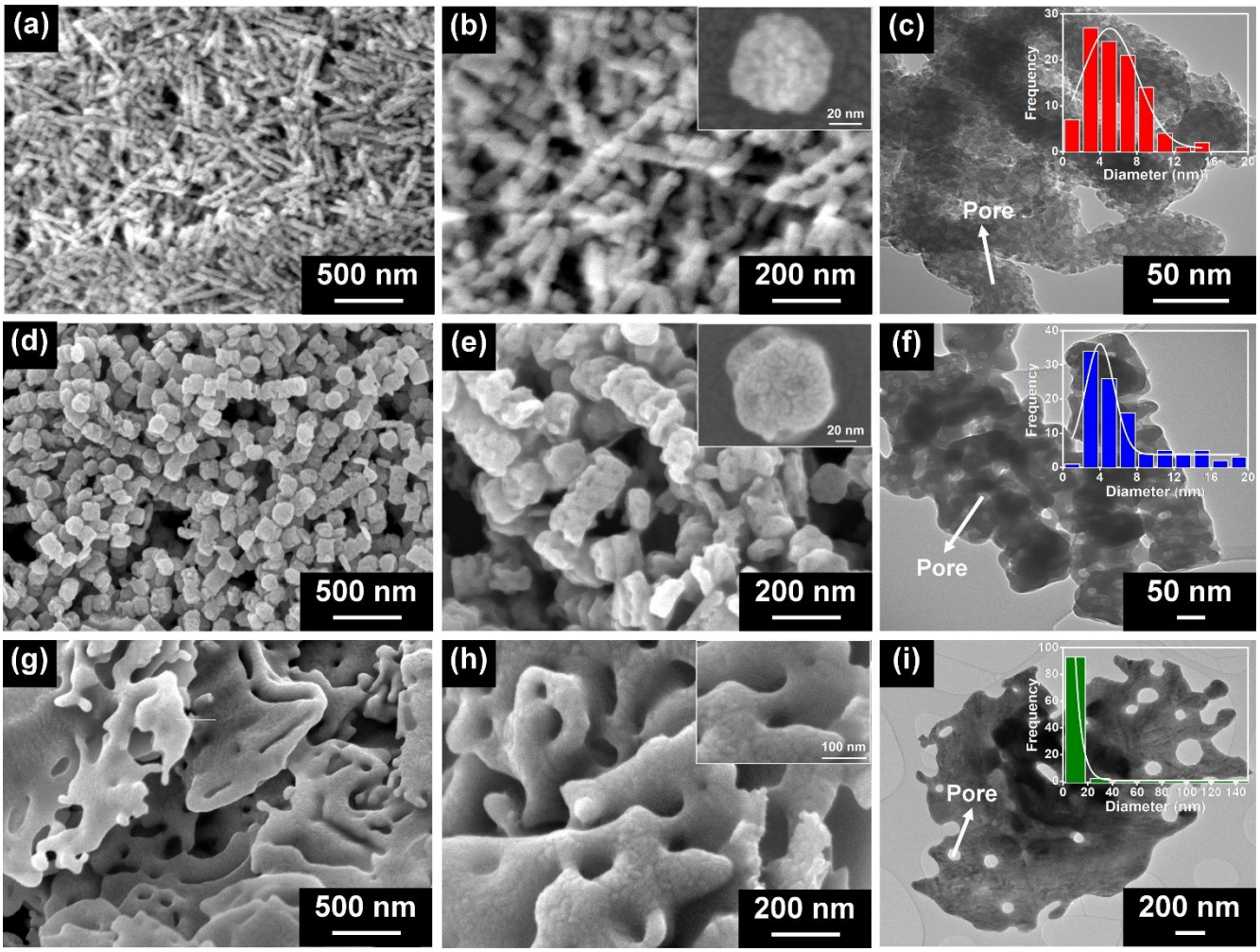

Figure 5. (a, b) SEM and (c) TEM images of Ni-TEP-600 (insets of (b) and (c) show the surface morphology and pore size distribution histogram of Ni-TEP-600). (d, e) SEM and (f) TEM images of Ni-Co-TEP-600 (insets of (d) and (e) show the surface morphology and pore size distribution histogram of Ni-Co-TEP-600).

(g, h) SEM and (i) TEM images of Co-TEP-600 (insets of (h) and (i) show the surface morphology and pore size distribution histogram of Co-TEP-600).

FTIR spectroscopy was used to further confirm the formation of metal phosphate species in the calcined metal-TEP samples. From **Figure 4b (i-iii)**, it can be observed that the calcined metal-TEP samples (Ni-TEP-600, Ni-Co-TEP-600, and Co-TEP-600) display very identical IR spectra. The broad peak between 3300-3500 cm^{-1} is assigned to the stretching vibration of O-H group, while the peaks at around 1050 and 930 cm^{-1} are indexed to the antisymmetric and symmetric stretching vibrations of PO_4^{3-}, respectively.[53] The peaks at 752, 754, and 751 cm^{-1} in the FTIR spectra of Ni-TEP-600, Ni-Co-TEP-600, and Co-TEP-600, respectively, can be assigned to the P-O-P stretching vibration.[54] Moreover, the peaks at 540, 548, and 546 cm^{-1} in the FTIR spectra of Ni-TEP-600, Ni-Co-TEP-600, and Co-TEP-600, respectively, are assignable to the out-of-plane bending mode of PO_4^{3-}.[55]

Figure 5 displays the SEM and TEM images of the products obtained by the calcination of Ni-TEP, Ni-Co-TEP, and Co-TEP precursors in air at 600 ^oC (*i.e.,* Ni-TEP-600, Ni-Co-TEP-600, and Co-TEP-600). As seen in **Figure 5a, b**, the Ni-TEP-600 product is highly uniform and retains the chain-like structure of the original Ni-TEP precursor. These chain-like particles formed by the assembly of fused nanoplates, as observed in **Figure S7a**. The SEM image of the single nanoplate assembling the chain-like Ni-TEP-600 particle reveals its hexagonal morphology and rough surface texture (**Figure S7b**). These chain-like particles exhibit numerous pores, as seen from the TEM image in **Figure 5c**. These pores are generated by the evaporation of organic by-products of TEP. The HRTEM image of Ni-TEP-600 (taken from the area inside the white box in **Figure S8a**) confirms the amorphous nature of this sample (**Figure S8b**), which is in good agreement with the XRD observation (**Figure 4a (i)**). Similar to Ni-TEP-600, the Ni-Co-TEP-600 product also shows a chain-like architecture which is assembled by the fusing of small nanoplates, as seen in **Figure 5d, e**. Compared to the Ni-Co-TEP precursor (pre-calcination), the chain-like Ni-Co-TEP-600 particles are considerably more porous (**Figure S7c, e**). SEM images of the single nanoplates assembling the chain-like Ni-Co-TEP and Ni-Co-TEP-600 particles clearly indicate the transition from a smooth hexagonal shape to a quasi-hexagonal shape with rough surface texture **(Figure S7d, f)**. The porous nature of these chain-like Ni-Co-TEP-600

particles is further supported by TEM images given in **Figure 5f** and **Figure S8c**. The corresponding HRTEM image of Ni-Co-TEP-600 shows its largely amorphous structure (**Figure S8d**), which is consistent with the XRD result in **Figure 4a (ii)**. In comparison, the Co-TEP-600 microplates exhibit many visible holes or macropores with sizes ranging from 50 to several hundred nanometers, as seen in **Figure 5g, h**. The holey structure of Co-TEP-600 can be further observed from the TEM images given in **Figure 5i** and **Figure S8e**. In contrast to Ni-TEP-600 and Ni-Co-TEP-600, the Co-TEP-600 product is highly crystalline as it shows clear lattice fringes with measured *d*-spacing of 0.321 nm and 0.302 nm, indexed to the (200) and ($\bar{1}$22) planes of CoP_2O_7 (**Figure S8f**). The average pore sizes of Ni-TEP-600, Ni-Co-TEP-600, and Co-TEP-600 are measured to be 8.8 nm, 18.8 and 113 nm, respectively (insets of **Figure 5c, f**, and **i**), based on a measurement of 100 different pores from the TEM images of the calcined metal-TEP samples.

The changes in morphology and porosity of the bimetallic Ni-Co-TEP sample with increasing calcination temperature are given in **Figure S9**. The Ni-Co-TEP-400 sample maintains the nanoplate-assembled chain-like morphology of the original Ni-Co-TEP precursor with some visible small pores on the surface of each nanoplate, originating from the initial decomposition of organic by-products of TEP (**Figure S9a**). In comparison, the Ni-Co-TEP-600 sample exhibits more visible pores resulting from further decomposition of these organic by-products. In addition, there is a greater degree of fusion between the nanoplates assembling the 1D chain-like particles at 600 °C (**Figure S9b**). However, at 800 °C, recrystallization of the Ni-Co phosphate occurs, leading to the complete fusion of the nanoplates into 1D chain-like structure with barely visible pores, as seen in **Figure S9c**. Although at 800 °C, better crystallinity can be obtained due to recrystallization of the metal phosphate products (based on the DTA curves in **Figure S6a-c**), the lack of pores and significant fusion of the particles at 800 °C will be disadvantageous for electrochemical applications. On the other hand, at 400 °C, the phase transformation to metal phosphate is not yet completed for Ni-TEP and Ni-Co-TEP samples (**Figure S6, b**). As such, we have selected 600 °C as the optimum calcination temperature for all TEP samples. In order to confirm the porous nature of the calcined metal-TEP products, N_2 adsorption-desorption measurements were carried out at 77 K. The BET specific surface areas (SSAs) of Ni-TEP-600, Ni-Co-TEP-600, and Co-TEP-600 are 52, 31, and 26 $m^2 g^{-1}$, respectively, with the corresponding pore volume being 0.78, 0.26, and 0.12 $cm^3 g^{-1}$ (**Figure S10**).

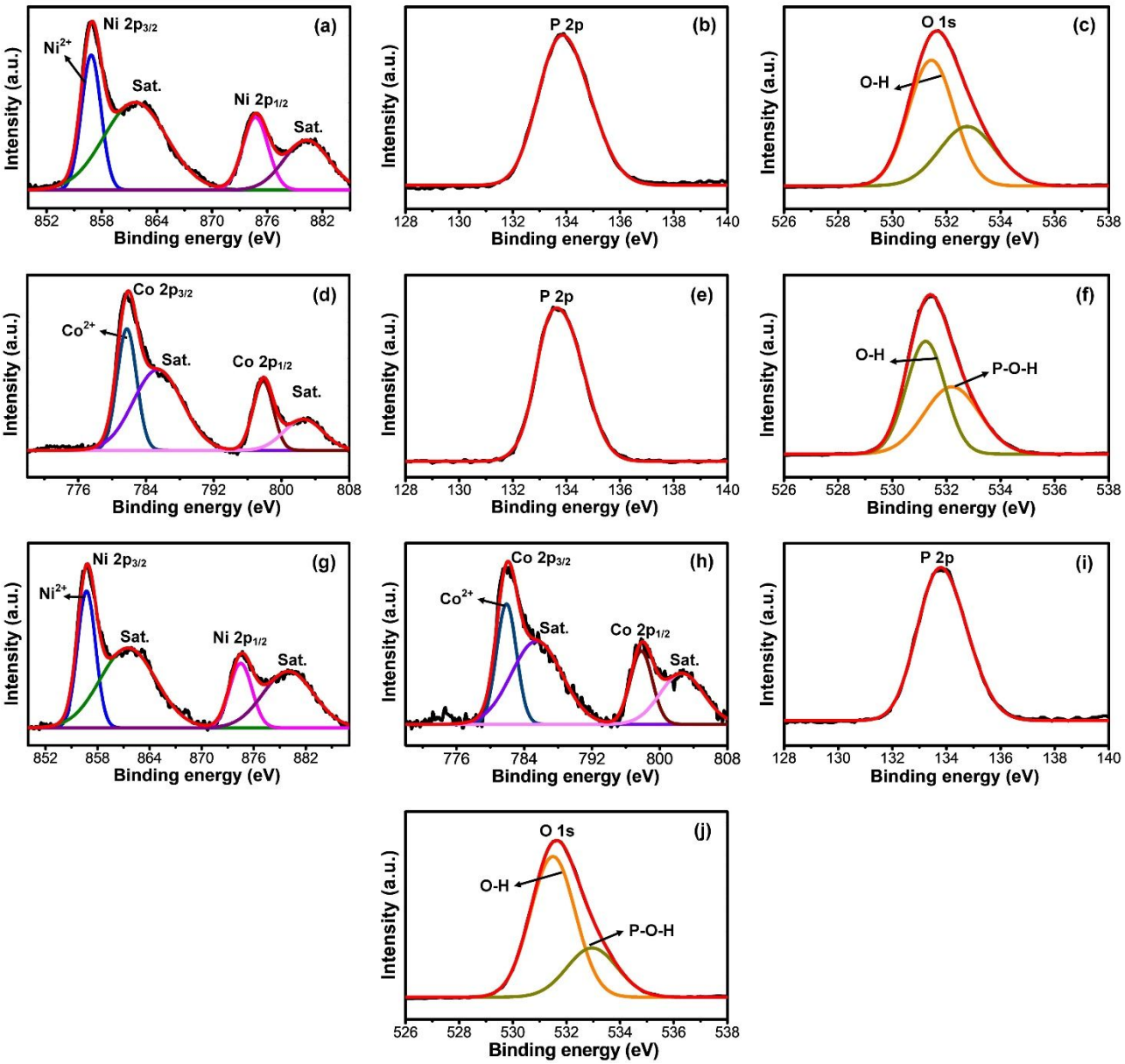

Figure 6. High-resolution Ni 2p (a), P 2p (b), and O 1s (c) spectra of Ni-TEP-600. High-resolution Co 2p (d), P 2p (e), and O 1s (f) spectra of Co-TEP-600. High-resolution Ni 2p (g), Co 2p (h), P 2p (i), and O 1s (j) spectra of Ni-Co-TEP-600.

XPS analysis was employed to investigate the surface elemental states of Ni-TEP-600, Ni-Co-TEP-600, and Co-TEP-600 (**Figure 6**). For Ni-TEP-600, the binding energies for Ni $2p_{3/2}$ and Ni $2p_{1/2}$ are centered at approximately 856.7 eV and 874.6 eV with two shake-up satellite peaks (862.0 eV and 880.5 eV), which correspond to Ni^{2+} species (**Figure 6a**).[56-57] The main peak centered at 133.8 eV in the high-resolution P 2p spectrum of Ni-TEP-600 is assigned to the P-O bond, which indicates the formation of phosphate species (**Figure 6b**).[58] The deconvoluted O 1s spectrum of Ni-TEP-600 reveals two peaks at 531.4 eV and 532.7 eV,

indexed to O-H and P-O-H species, respectively (**Figure 6c**). In the case of Co-TEP-600, the high-resolution Co 2p spectrum displays two distinct peaks at 781.70 eV and 797.80 eV, assigned to Co $2p_{3/2}$ and Co $2p_{1/2}$, respectively (**Figure 6d**). The binding energy difference between the Co $2p_{3/2}$ and Co $2p_{1/2}$ peaks is 16.1 eV, which is indicative of Co^{2+} species. For Co-TEP-600, the P 2p peak is centered at around 133.7 eV, indicating the pentavalent state of phosphorus in this sample and supports the presence of phosphate species (**Figure 6e**). Similar to Ni-TEP-600, the high-resolution O 1s spectrum of Co-TEP-600 also shows two peaks indexed to O-H and P-O-H species at 531.2 eV and 532.3 eV, respectively (**Figure 6f**). In the case of Ni-Co-TEP-600, the high-resolution Ni 2p spectrum features two peaks at 856.7 eV and 874.7 eV, corresponding to Ni $2p_{3/2}$ and Ni $2p_{1/2}$, respectively (**Figure 6g**). These peaks indicate the Ni^{2+} state of the Ni species in Ni-Co-TEP-600.[56-57] The Co $2p_{3/2}$ and Co $2p_{1/2}$ peaks of Ni-Co-TEP-600 are located at 782.1 eV and 798.0 eV, respectively (**Figure 6h**), with a binding energy difference of 15.9 eV, which is indicative of Co^{2+}. The presence of phosphate species in Ni-Co-TEP-600 is indicated by the single intense peak at 133.8 eV (**Figure 6i**). The deconvoluted O 1s spectrum of Ni-Co-TEP-600 also reveals two main peaks indexed to O-H and P-O-H at 531.5 eV and 532.9 eV, respectively (**Figure 6j**).

3.2. OER performance

Inspired by the unique self-assembled architectures, the electrocatalytic activities of Ni-TEP-600, Ni-Co-TEP-600, and Co-TEP-600 towards oxygen evolution reaction (OER) were evaluated in 1.0 M KOH electrolyte. The linear sweep voltammetry (LSV) curves of the three catalysts (normalized by geometric surface area) are presented in **Figure 7a**. A strong peak is observed at 1.35 V for the bimetallic Ni-Co-TEP-600 catalyst which may be attributed to the oxidation of Co species from Co^{2+} to Co^{3+} (based on post-OER XPS analysis below). The onset potential is defined as the potential at which the current starts to increase. From the LSV curves, the onset potentials of Ni-TEP-600, Ni-Co-TEP-600, and Co-TEP-600 are determined to be 1.54 V, 1.49, and 1.56 V, respectively. The overpotentials required to produce a current density of 10 mA cm^{-2} (η_{10}) are 400 mV, 340 mV, and 310 mV for Ni-TEP-600, Co-TEP, and Ni-Co-TEP-600, respectively. The OER kinetics of the catalysts were evaluated by deriving Tafel plots from the LSV curves. As seen in **Figure 7b**, the Tafel

slope of the Ni-Co-TEP-600 catalyst is 68 mVdec^{-1}, which is lower than those of Ni-TEP-600 (141 mV dec^{-1}) and Co-TEP-600 (74 mV dec^{-1}), respectively.

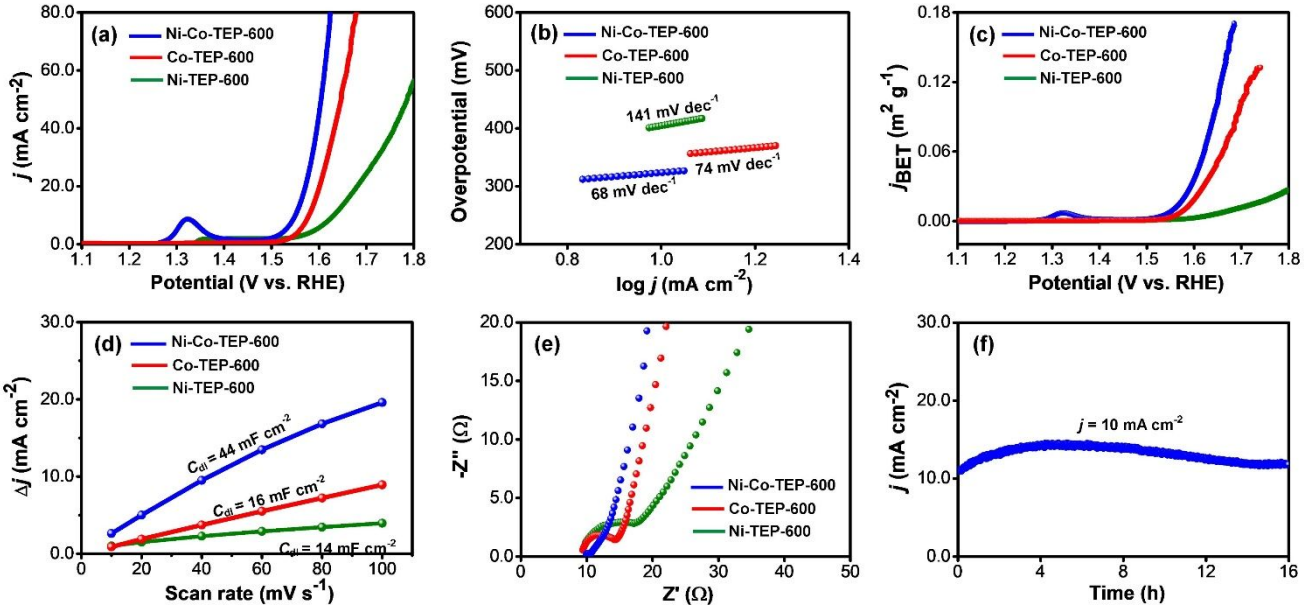

Figure 7. (a) LSV curves (normalized by geometric surface area), (b) Tafel plots, and (c) BET surface area-normalized LSV curves of Ni-TEP-600, Co-TEP-600, Ni-Co-TEP-600. (d) Capacitive currents as a function of scan rate plots of Ni-TEP-600, Co-TEP-600, and Ni-Co-TEP-600 towards OER in 1.0 M KOH solution. (e) Nyquist plots of Ni-TEP-600, Co-TEP-600, and Ni-Co-TEP-600 at a potential of 1.4 *versus* RHE. (f) Stability test of the Ni-Co-TEP-600 for OER in 1.0 M KOH solution at a fixed overpotential of 310 mV for 16 h.

The BET surface area-normalized LSV curves shown in **Figure 7c** indicate that the intrinsic activity for OER is in the order of Ni-Co-TEP-600> Co-TEP-600 > Ni-TEP-600, which is good agreement with the geometric surface area-normalized LSV curves. This finding confirms the superior intrinsic catalytic activity of the bimetallic Ni-Co phosphate (Ni-Co-TEP-600) catalyst for OER compared to its pristine counterparts (Ni-TEP-600 and Co-TEP-600). The corresponding BET surface area-normalized current densities of the Ni-Co-TEP-600, Ni-TEP-600, and Co-TEP-600 catalysts at a potential of 1.6 V (*versus* RHE) are 0.0354, 0.0179, and 0.00357 mA cm^{-2}, respectively. Furthermore, as summarized in **Table S3**, the Ni-Co-TEP-600 catalyst exhibits better catalytic activity for OER compared to Ni-Co phosphate plates,[58] 1D and 2D CoP_2PO_7

nanostructures,[30] ordered mesoporous cobalt phosphate,[27] $NaCo(PO_3)_3$/graphitized carbon hybrid,[59] flower-like cobalt-zinc phosphate,[4] and $(Fe_4Co_1)P_2O_7$@N-C hybrid.[60]

It has been previously reported that the OER activity is influenced by several factors, including specific surface area, electrochemical active surface area (ECSA), charge transfer, and the electronic structure of the surface of the catalyst.[32] The superior activity of the Ni-Co-TEP-600 catalyst may be attributed to several factors. One of the important parameters affecting the performance of an OER catalyst is the electrochemical active surface area (ESCA). Higher ECSA implies a larger number of active sites present on the catalyst. This parameter is represented by the electrochemical double-layer capacitance (C_{dl}) which can be obtained from the CV curves. The CV measurements were performed in 1.0 M KOH solution in the potential range of 1.34-1.44 *versus* RHE at various scan rates from 10 to 100 mV s^{-1}. The C_{dl} values were determined from half of the slopes of current density *versus* scan rate plots. As evident in **Figure 7d**, the Ni-Co-TEP-600 catalyst has around 2-3 times higher ECSA (44.0 mF cm^{-2}) than Ni-TEP-600 (12 mF cm^{-2}) and Co-TEP-600 (16 mF cm^{-2}). This trend indicates the larger number of electrochemical active sites on the bimetallic Ni-Co-TEP-600 catalyst than on Ni-TEP-600 and Co-TEP-600, which accounts for its superior OER activity. The trend in ECSA is notably different from the trend in BET specific surface area, as unlike BET, the ECSA is influenced by a combination of various factors, such as potential and testing conditions, including electrolyte pH and electron conductivity.[61] Furthermore, a previous study found that there were no strict correlations between BET specific surface area and ECSA for many transition metal-based catalysts.[62]

The second reason behind the superior activity of the Ni-Co-TEP-600 catalyst is its lower charge transfer resistance compared to both Ni-TEP-600 and Co-TEP-600 catalysts, as seen in **Figure 7e**. The lower charge transfer resistance of the Ni-Co-TEP-600 catalyst may be attributed to its nanoplate-assembled chain-like structure which can provide good interconnection between the particles to enable fast electron transport and the bimetallic composition which can promote improved conductivity. The presence of numerous pores on the Ni-Co-TEP-600 catalyst may facilitate easier electrolyte infiltration into the chain-like structures and promotes good electrical contact with the electrolyte, therefore enhancing the overall surface reactions.[63] The stability of the optimum catalyst (Ni-Co-TEP-600) was checked by chronoamperometric measurement for 16 h at a fixed overpotential of 310 mV. As shown in **Figure 7f**, the current density increases over the first 4 h

due to surface activation (from the formation of active metal (oxy)hydroxide species, as supported by the post-OER XPS analysis below) before decreasing to reach a stable state. However, the current density never drops below 10.0 mA cm^{-2} throughout the measurement. This indicates the good electrochemical stability of the bimetallic Ni-Co-TEP-600 catalyst.

To gain additional insights into the active sites, post-OER XPS analysis of the best catalyst (Ni-Co-TEP-600) was performed and comparison of the XPS spectra of Ni-Co-TEP-600 before and after cycling is given in **Figure S11a-h**. As shown in **Figure S11b**, the post-OER Ni 2p spectrum of the Ni-Co-TEP-600 catalyst reveals the formation of Ni^{3+} species (NiOOH), as indicated by the negative shifts of Ni $2p_{3/2}$ and Ni $2p_{1/2}$ peaks to lower binding energies of 856.0 eV and 873.7 eV, respectively. Similarly, the Co^{2+} species is also partially converted to Co^{3+} species (CoOOH), after cycling, as verified by the appearance of Co $2p_{3/2}$ and Co $2p_{1/2}$ peaks at 780.6 eV and 796.2 eV (corresponding to Co^{3+}), respectively, while the Co^{2+} peak intensity is severely reduced compared to that prior to the stability test (**Figure S11c, d**).[64-65] This confirms that during OER, the conversion of some Co^{2+} species to Co^{3+} (CoOOH) took place. The complete disappearance of the P 2p signal is observed after cycling, as seen in **Figure S11f**. Further, the post-OER O 1s spectrum reveals an increase in the intensity of the O-H peak, accompanied by a considerable reduction in the intensity of the P-O-H peak (**Figure S11h)**.[66] These results indicate that the real catalytic sites may originate from the phosphate-derived Ni-Co oxyhydroxide.[67] Transition metal cations with high oxidation states, (*e.g.*, Ni^{3+} and Co^{3+} present in Ni-Co-TEP-600) have been widely reported to be active sites for OER owing to their lower coordination numbers which can promote the chemisorption of OH^- and facilitate the electron transfer from the OH^- to the surface Ni/Co sites during OER.[63, 68-69] Furthermore, these high-valent Ni and Co species have been reported to exhibit enhanced electrophilicity[70] and promote the deprotonation of OOH species to form O_2.[63] In addition, the presence of Ni cations in the cobalt oxyhydroxide system can synergistically enhance the OER activity according to previous DFT simulation studies.[71-72] It has been reported that the phosphate group on the surface of metal phosphate-based catalysts may cause distortion of the nickel or cobalt geometry, which increases the stability from the Jahn-Teller effect and enhances the electronic interactions between Ni and Co metals and oxygen, thereby accelerating the rate of oxygen evolution.[73-75]

The post-OER SEM images of the metal phosphate-based catalysts (*i.e.*, Ni-TEP-600, Ni-Co-TEP-600, and Co-TEP-600) are given in **Figure 8**. From **Figure 8a-i**, it can be observed that chain-like architectures of the Ni-TEP-600 and Ni-Co-TEP catalysts, as well as the microplate structure of the Co-TEP-600 catalyst, are well-retained after the OER measurement. Interestingly, the formation of sheet-like structures is observed on the surface of both Ni-Co-TEP-600 and Co-TEP-600 catalysts after OER (**Figure 8d-i**), which supports the formation of active metal (oxy)hydroxide species on the surface of these catalysts, as identified earlier by XPS (**Figure S10**). In contrast, no significant change is observed on the surface of the Ni-TEP-600 catalyst after OER (**Figure 8a-c**), which indicates the limited presence of metal (oxy)hydroxide species. This may explain the lower activity of Ni-TEP-600 for OER compared to Ni-Co-TEP-600 and Co-TEP-600. The high structural stability of the chain-like Ni-Co-TEP-600 particles accounts for the good electrochemical stability of this catalyst for OER (**Figure 7f**).

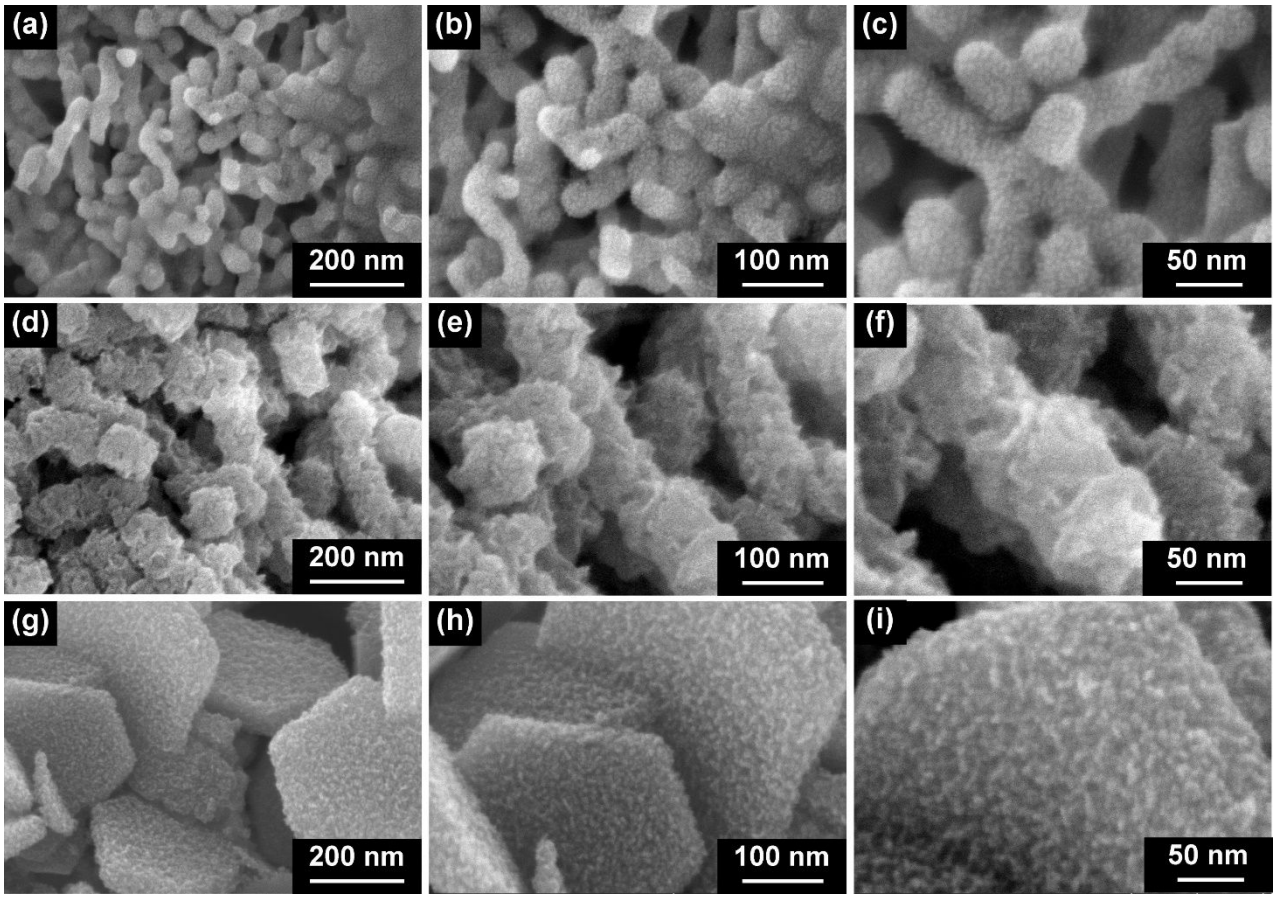

Figure 8. Post-OER SEM images of (a) Ni-TEP-600, (b) Ni-Co-TEP-600, and (c) Co-TEP-600 catalysts.

4. Conclusions

In summary, this work has demonstrated the successful self-assembly of 2D bimetallic Ni-Co phosphate nanoplates into porous 1D chain-like particles through the mild solvothermal reaction of Ni-Co glycerate particles (as self-templates) with TEP, followed by post-synthetic calcination in air at 600 °C. The unique self-stacking phenomenon is believed to be promoted by the adsorption of ethyl glycerate on the surface of the nanoplates, which confines the growth of the new nanoplate on top of the previously formed nanoplate. The electrochemical measurements reveal the lower overpotential and Tafel slope of the optimum Ni-Co-TEP-600 catalyst (310 mV and 68 mV dec^{-1}) compared to Co-TEP-600 (340 mV and 74 mV dec^{-1}) and Ni-TEP-600 (400 mV and 141 mV dec^{-1}). The BET-normalized LSV curves reveal that the intrinsic activity for OER is in the order of Ni-Co-TEP-600 > Co-TEP-600 > Ni-TEP-600, thus confirming the superior activity of the bimetallic Ni-Co phosphate catalyst for OER. The enhanced OER activity of this bimetallic catalyst compared to its pristine counterparts may be attributed to (i) the increased number of active sites (as evidenced by its higher ECSA); (ii) lower charge transfer resistance (as supported by the EIS measurements) due to the bimetallic composition and the nanoplate-assembled chain-like structure which can provide improved charge transport, and (iii) the formation of active Ni-Co (oxy)hydroxide species on its surface (as identified by post-OER XPS analysis). More importantly, the Ni-Co-TEP-600 catalyst exhibits good stability for OER with negligible change in current density after 16 h of continuous cycling as a result of the high structural stability of the chain-like structure (based on the post-OER SEM analysis). It is expected that the proposed template-assisted strategy may provide a useful method for producing novel 2D nanomaterials which are uniquely assembled of 1D nanostructures for a wide variety of applications, such as catalysis, energy storage and conversion, sensors, and so on.

Acknowledgements

D. G. is grateful to the Australian Research Council (ARC) for granting a Laureate Fellowship (FL160100089) and to QUT projects Nos. 323000-0355/51 and 323000-0348/07. The authors also acknowledge financial grants provided by Institute of Technology Bandung (ITB), the Ministry of Education and Culture and Ministry of Research and Technology under the grant scheme of the World Class University (WCU) Program

managed by Institut Teknologi Bandung, Lembaga Pengelola Dana Pendidikan (LPDP), and Ministry of Finance of Indonesia. The authors thank Bill Gong from the UNSW Mark Wainwright Analytical Center for the XPS measurements and discussion. This work was partially supported by the Researchers Supporting Project No. (RSP-2020/1) King Saud University, Riyadh, Saudi Arabia. This work was performed in part at the Queensland node of the Australian National Fabrication Facility (ANFF), a company established under the National Collaborative Research Infrastructure Strategy to provide nano and microfabrication facilities for Australian researchers.

Associated Content

Supporting Information

The Supporting Information is available free of charge on the ACS Publications. XRD patterns of metal glycerate precursors; FTIR spectra comparison of TEP and Ni-Co-TEP; FTIR spectra comparison of nickel glycerate and Ni-TEP; ICP analyses of Ni-TEP, Co-TEP, and Ni-Co-TEP; FTIR spectrum of supernatant collected after the solvothermal reaction; SEM images of the product obtained using $Ni(NO_3)_2{\cdot}6H_2O$ and $Co(NO_3)_2{\cdot}6H_2O$ as Ni and Co sources and TEP at 180 °C for 16 h; TG-DTA curves of Ni-TEP (a), Ni-Co-TEP (b), and Co-TEP; Crystallographic data of CoP_2O_7 according to ICSD No. 84-2126; SEM images of chain-like Ni-TEP-600, Ni-Co-TEP, and Ni-Co-TEP-600 and the assembling nanoplates; TEM and HRTEM images of Ni-TEP-600, Ni-Co-TEP-600, and Co-TEP-600; SEM images of the products achieved by calcination of Ni-Co-TEP particles at 400 ^oC, 600 ^oC, and (c) 800 ^oC; N_2 adsorption-desorption isotherms of Ni-TEP-600, Ni-Co-TEP-600, and Co-TEP-600; Comparison of the OER performance of the Ni-Co-TEP-600 catalyst with previously reported phosphate-based catalysts; XPS data of the Ni-Co-TEP-600 catalyst before and after cycling for OER.

Notes

The authors declare no competing financial interest.

Corresponding Authors

Email: KANETI.Valentino@nims.go.jp

Email brian@tf.itb.ac.id

Email: dmitry.golberg@qut.edu.au

Email: y.yamauchi@uq.edu.au

ORCID

Yusuf Valentino Kaneti: 0000-0003-2433-7305

Brian Yuliarto: 0000-0003-0662-7923

Hermawan Kresno Dipojono: 0000-0002-1391-3533

Zeid A. Alothman: 0000-0001-9970-2480

Dmitri Golberg: 0000-0003-2298-6539

Yusuke Yamauchi: 0000-0001-7854-927X

References

1. Thorkelsson, K.; Bai, P.; Xu, T., Self-Assembly and Applications of Anisotropic Nanomaterials: A Review. *Nano Today* **2015,** *10*, 48-66.

2. Ma, Q.; Wang, Y.; Kong, J.; Jia, H.; Wang, Z., Controllable Synthesis of Hierarchical Flower-Like ZnO Nanostructures Assembled by Nanosheets and Its Optical Properties. *Superlattices Microstruct.* **2015,** *84*, 1-12.

3. Kaneti, Y. V.; Yue, J.; Moriceau, J.; Chen, C.; Liu, M.; Yuan, Y.; Jiang, X.; Yu, A., Experimental and Theoretical Studies on Noble Metal Decorated Tin Oxide Flower-Like Nanorods with High Ethanol Sensing Performance. *Sens. Actuators B* **2015,** *219*, 83-93.

4. Zhang, H.; Du, X.; Ding, S.; Wang, Q.; Chang, L.; Ma, X.; Hao, X.; Pen, C., DFT Calculations of the Synergistic Effect of λ-MnO_2/Graphene Composites for Electrochemical Adsorption of Lithium Ions. *Phys. Chem. Chem. Phys.* **2019,** *21*, 8133-8140.

5. Zhou, X.; Du, H.; Ma, H.; Sun, L.; Cao, R.; Li, H.; Zhang, P., Facile Preparation and Characterization of Zinc Phosphate with Self-Assembled Flower-Like Micro-Nanostructures. *J. Phys. Chem. Solids* **2015,** *78*, 1-7.

6. Wang, Q.; Lian, J.; Li, J.; Wang, R.; Huang, H.; Su, B.; Lei, Z., Highly Efficient Photocatalytic Hydrogen Production of Flower-like Cadmium Sulfide Decorated by Histidine. *Sci. Rep.* **2015,** *5*, 13593.

7. Zhai, M.; Cheng, Y.; Jin, Y.; Hu, J., Solvothermal Synthesis of Flower-Like Structure Cu-Mn Bimetallic Sulfide on Ni-Foam for High-Performance Symmetric Supercapacitors. *Int. J. Hydrog. Energy* **2019,** *44*, 13456-13465.

8. Li, G.; Zhang, X.; Zhang, H.; Liao, C.; Jiang, G., Bottom-Up MOF-Intermediated Synthesis of 3D Hierarchical Flower-Like Cobalt-Based Homobimetallic Phophide Composed of Ultrathin Nanosheets for Highly Efficient Oxygen Evolution Reaction. *Appl. Catal. B* **2019,** *249*, 147-154.

9. Wang, W.; Li, J.; Bi, M.; Zhao, Y.; Chen, M.; Fang, Z., Dual Function Flower-Like CoP/C Nanosheets: High Stability Lithium-Ion Anode and Excellent Hydrogen Evolution Reaction Catalyst. *Electrochim. Acta* **2018,** *259*, 822-829.

10. Cao, J.; Mei, Q.; Wu, R.; Wang, W., Flower-Like Nickel–Cobalt Layered Hydroxide Nanostructures for Super Long-Life Asymmetrical Supercapacitors. *Electrochim. Acta* **2019,** *321*, 134711.

11. Hou, L.; Du, Q.; Su, L.; Di, S.; Ma, Z.; Chen, L.; Shao, G., Ni-Co Layered Double Hydroxide with Self-Assembled Urchin Like Morphology for Asymmetric Supercapacitors. *Mater. Lett.* **2019,** *237*, 262-265.

12. Zhang, X.; Lv, L.; Ji, L.; Guo, G.; Liu, L.; Han, D.; Wang, B.; Tu, Y.; Hu, J.; Yang, D.; Dong, A., Self-Assembly of One-Dimensional Nanocrystal Superlattice Chains Mediated by Molecular Clusters. *J. Am. Chem. Soc.* **2016,** *138*, 3290-3293.

13. Li, T.; Wang, B.; Ning, J.; Li, W.; Guo, G.; Han, D.; Xue, B.; Zou, J.; Wu, G.; Yang, Y.; Dong, A.; Zhao, D., Self-Assembled Nanoparticle Supertubes as Robust Platform for Revealing Long-Term, Multiscale Lithiation Evolution. *Matter* **2019,** *1*, 976-987.

14. Lai, Z.; Chen, Y.; Tan, C.; Zhang, X.; Zhang, H., Self-Assembly of Two-Dimensional Nanosheets into One-Dimensional Nanostructures. *Chem* **2016,** *1*, 59-77.

15. Septiani, N. L. W.; Kaneti, Y. V.; Guo, Y.; Yuliarto, B.; Jiang, X.; Ide, Y.; Nugraha, N.; Dipojono, H. K.; Yu, A.; Sugahara, Y.; Golberg, D.; Yamauchi, Y., Holey Assembly of Two-Dimensional Iron-Doped Nickel-Cobalt Layered Double Hydroxide Nanosheets for Energy Conversion Application. *ChemSusChem* **2019,** *13*,1645-1655.

16. Dutta, S.; Indra, A.; Feng, Y.; Song, T.; Paik, U., Self-Supported Nickel Iron Layered Double Hydroxide-Nickel Selenide Electrocatalyst for Superior Water Splitting Activity. *ACS Appl. Mater. Interfaces* **2017,** *9*, 33766-33774.

17. Wang, T.-J.; Liu, X.; Li, Y.; Li, F.; Deng, Z.; Chen, Y., Ultrasonication-Assisted and Gram-Scale Synthesis of Co-LDH Nanosheet Aggregates for Oxygen Evolution Reaction. *Nano Res.* **2020,** *13*, 79-85.

18. You, B.; Zhang, Y.; Yin, P.; Jiang, D.-e.; Sun, Y., Universal Molecular-Confined Synthesis of Interconnected Porous Metal Oxides-N-C Frameworks for Electrocatalytic Water Splitting. *Nano Energy* **2018,** *48*, 600-606.

19. Zhuang, M.; Liu, Z.; Ding, Y.; Xu, G.-L.; Li, Y.; Tyagi, A.; Zhang, X.; Sun, C.-J.; Ren, Y.; Ou, X.; Wong, H.; Cai, Y.; Wu, R.; Abidi, I. H.; Zhang, Q.; Xu, F.; Amine, K.; Luo, Z., Methacrylated Gelatin-Embedded Fabrication of 3D Graphene-Supported Co_3O_4 Nanoparticles for Water Splitting. *Nanoscale* **2019,** *11*, 6866-6875.

20. Fu, H.; Liu, Y.; Chen, L.; Shi, Y.; Kong, W.; Hou, J.; Yu, F.; Wei, T.; Wang, H.; Guo, X., Designed Formation of $NiCo_2O_4$ with Different Morphologies Self-Assembled from Nanoparticles for Asymmetric Supercapacitors and Electrocatalysts for Oxygen Evolution Reaction. *Electrochim. Acta* **2019,** *296*, 719-729.

21. Guo, Y.; Tang, J.; Wang, Z.; Kang, Y.-M.; Bando, Y.; Yamauchi, Y., Elaborately Assembled Core-Shell Structured Metal Sulfides as a Bifunctional Catalyst for Highly Efficient Electrochemical Overall Water Splitting. *Nano Energy* **2018,** *47*, 494-502.

22. Guo, Y.; Tang, J.; Qian, H.; Wang, Z.; Yamauchi, Y., One-Pot Synthesis of Zeolitic Imidazolate Framework 67-Derived Hollow Co_3S_4@MoS_2 Heterostructures as Efficient Bifunctional Catalysts. *Chem. Mater.* **2017,** *29*, 5566-5573.

23. Prabakaran, K.; Ingavale, S. B.; Kakade, B., Three Dimensional NiS_2–$Ni(OH)_2$/CNT Nanostructured Assembly for Supercapacitor and Oxygen Evolution Reaction. *J. Alloys Compd.* **2020,** *812*, 152126.

24. Xie, J.-Y.; Liu, Z.-Z.; Li, J.; Feng, L.; Yang, M.; Ma, Y.; Liu, D.-P.; Wang, L.; Chai, Y.-M.; Dong, B., Fe-Doped CoP Core–Shell Structure with Open Cages as Efficient Electrocatalyst for Oxygen Evolution. *J. Energy Chem.* **2020,** *48*, 328-333.

25. Shanmugam, S.; Sivanantham, A.; Matsunaga, M.; Simon, U.; Osaka, T., Metal Phosphide Nanoparticles Embedded in Carbon as Efficient Electrocatalyst for Oxygen Evolution Reaction. *Electrochim. Acta* **2019,** *297*, 749-754.

26. Guo, Y.; Tang, J.; Wang, Z.; Sugahara, Y.; Yamauchi, Y., Hollow Porous Heterometallic Phosphide Nanocubes for Enhanced Electrochemical Water Splitting. *Small* **2018,** *14*, 1802442.

27. Pramanik, M.; Li, C.; Imura, M.; Malgras, V.; Kang, Y.-M.; Yamauchi, Y., Ordered Mesoporous Cobalt Phosphate with Crystallized Walls toward Highly Active Water Oxidation Electrocatalysts. *Small* **2016,** *12*, 1709-1715.

28. Septiani, N. L. W.; Kaneti, Y. V.; Fathoni, K. B.; Guo, Y.; Ide, Y.; Yuliarto, B.; Jiang, X.; Nugraha; Dipojono, H. K.; Golberg, D.; Yamauchi, Y., Tailorable Nanoarchitecturing of Bimetallic Nickel–Cobalt Hydrogen Phosphate via the Self-Weaving of Nanotubes for Efficient Oxygen Evolution. *J. Mater. Chem. A* **2020,** *8*, 3035-3047.

29. Qian, L.; Miao, Y., Nanosheet Organized Flower-Like Co/Zn Phosphate on Nickel Foam for Efficient Water Splitting in Both Acid and Basic Solutions. *Polyhedron* **2019,** *160*, 213-218.

30. Du, H.; Ai, W.; Zhao, Z. L.; Chen, Y.; Xu, X.; Zou, C.; Wu, L.; Su, L.; Nan, K.; Yu, T.; Li, C. M., Engineering Morphologies of Cobalt Pyrophosphates Nanostructures toward Greatly Enhanced Electrocatalytic Performance of Oxygen Evolution Reaction. *Small* **2018,** *14*, 1801068.

31. Kaneti, Y. V.; Salunkhe, R. R.; Wulan Septiani, N. L.; Young, C.; Jiang, X.; He, Y.-B.; Kang, Y.-M.; Sugahara, Y.; Yamauchi, Y., General Template-Free Strategy for Fabricating Mesoporous Two-Dimensional Mixed Oxide Nanosheets via Self-Deconstruction/Reconstruction of Monodispersed Metal Glycerate Nanospheres. *J. Mater. Chem. A* **2018,** *6*, 5971-5983.

32. Septiani, N. L. W.; Kaneti, Y. V.; Guo, Y.; Yuliarto, B.; Jiang, X.; Ide, Y.; Nugraha, N.; Dipojono, H. K.; Yu, A.; Sugahara, Y.; Golberg, D.; Yamauchi, Y., Holey Assembly of Two-Dimensional Iron-Doped Nickel-Cobalt Layered Double Hydroxide Nanosheets for Energy Conversion Application. *ChemSusChem* **2020,** *13*, 1645.

33. Kaneti, Y. V.; Wulan Septiani, N. L.; Saptiama, I.; Jiang, X.; Yuliarto, B.; Shiddiky, M. J. A.; Fukumitsu, N.; Kang, Y.-M.; Golberg, D.; Yamauchi, Y., Self-Sacrificial Templated Synthesis of a Three-Dimensional Hierarchical Macroporous Honeycomb-Like ZnO/$ZnCo_2O_4$ Hybrid for Carbon Monoxide Sensing. *J. Mater. Chem. A* **2019,** *7*, 3415-3425.

34. Ren, H.; Pan, Y.; Sorrell, C. C.; Du, H., Assessment of Electrocatalytic Activity Through the Lens of Three Surface Area Normalization Techniques. *J. Mater. Chem. A* **2020,** *8*, 3154-3159.

35. Taddei, M.; Sassi, P.; Costantino, F.; Vivani, R., Amino-Functionalized Layered Crystalline Zirconium Phosphonates: Synthesis, Crystal Structure, and Spectroscopic Characterization. *Inorg. Chem.* **2016,** *55*, 6278-6285.

36. Zhang, F.; Bao, Y.; Ma, S.; Liu, L.; Shi, X., Hierarchical Flower-Like Nickel Phenylphosphonate Microspheres and Their Calcined Derivatives for Supercapacitor Electrodes. *J. Mater. Chem. A* **2017,** *5*, 7474-7481.

37. B. Hix, G.; D. M. Harris, K., Synthesis of Layered Nickel Phosphonate Materials Based on a Topotactic Approach. *J. Mater. Chem.* **1998,** *8*, 579-584.

38. George, L.; Sankaran, K.; Viswanathan, K. S.; Mathews, C. K., Matrix-Isolation Infrared Spectroscopy of Organic Phosphates. *Appl. Spectrosc.* **1994,** *48*, 7-12.

39. Kaya, N.; Bardakçı, B., FT-IR Spectroscopic Study of Triethyl Phosphate Adsorption on FAU Type Zeolite. *Asian J. Chem.* **2009,** *21*, 4914-4919.

40. Mäkie, P.; Persson, P.; Österlund, L., Adsorption of Trimethyl Phosphate and Triethyl Phosphate on Dry and Water Pre-Covered Hematite, Maghemite, and Goethite Nanoparticles. *J. Colloid Interface Sci.* **2013,** *392*, 349-358.

41. Mäkie, P.; Westin, G.; Persson, P.; Österlund, L., Adsorption of Trimethyl Phosphate on Maghemite, Hematite, and Goethite Nanoparticles. *J. Phys. Chem. A* **2011,** *115*, 8948-8959.

42. Santana, M. D.; García, G.; Lozano, A. A.; López, G.; Tudela, J.; Pérez, J.; García, L.; Lezama, L.; Rojo, T., Pentacoordinate Nickel(II) Complexes Double Bridged by Phosphate Ester or Phosphinate Ligands: Spectroscopic, Structural, Kinetic, and Magnetic Studies. *Chem.-Euro. J* **2004,** *10*, 1738-1746.

43. Liang, Q.; Shi, Y.; Ma, W.; Li, Z.; Yang, X., Enhanced Photocatalytic Activity and Structural Stability by Hybridizing Ag_3PO_4 Nanospheres with Graphene Oxide Sheets. *Phys. Chem. Chem. Phys.* **2012,** *14*, 15657-15665.

44. Sun, C.; Xu, D.; Xue, D., Direct In Situ ATR-IR Spectroscopy of Structural Dynamics of $NH_4H_2PO_4$ in Aqueous Solution. *CrystEngComm* **2013,** *15*, 7783-7791.

45. Anupama, B.; Sunita, M.; Shiva Leela, D.; Ushaiah, B.; Gyana Kumari, C., Synthesis, Spectral Characterization, DNA Binding Studies and Antimicrobial Activity of Co(II), Ni(II), Zn(II), Fe(III) and VO(IV) Complexes with 4-Aminoantipyrine Schiff Base of Ortho-Vanillin. *J. Fluoresc.* **2014,** *24*, 1067-1076.

46. Xu, Z.-H.; Chen, F.-J.; Xi, P.-X.; Liu, X.-H.; Zeng, Z.-Z., Synthesis, Characterization, and DNA-Binding Properties of the Cobalt(II) and Nickel(II) Complexes with Salicylaldehyde 2-Phenylquinoline-4-Carboylhydrazone. *J. Photochem. Photobio.* **2008,** *196*, 77-83.

47. Fouad, O. A.; Makhlouf, S. A.; Ali, G. A. M.; El-Sayed, A. Y., Cobalt/Silica Nanocomposite via Thermal Calcination-Reduction of Gel Precursors. *Mater. Chem. Phys.* **2011,** *128*, 70-76.

48. Tang, C.-W.; Wang, C.-B.; Chien, S.-H., Characterization of Cobalt Oxides Studied by FT-IR, Raman, TPR and TG-MS. *Thermochim. Acta* **2008,** *473*, 68-73.

49. Calandra, P.; de Caro, T.; Caschera, D.; Lombardo, D.; Todaro, L.; Turco Liveri, V., Spectroscopic and Structural Characterization of Pure and $FeCl_3$-Containing Tri-n-Butyl Phosphate. *Colloid Polym. Sci.* **2015,** *293*, 597-603.

50. Schnaidt, J.; Heinen, M.; Denot, D.; Jusys, Z.; Jürgen Behm, R., Electrooxidation of Glycerol Studied by Combined In Situ IR Spectroscopy and Online Mass Spectrometry under Continuous Flow Conditions. *J. Electroanal. Chem.* **2011,** *661*, 250-264.

51. Oliveira, V. L.; Morais, C.; Servat, K.; Napporn, T. W.; Tremiliosi-Filho, G.; Kokoh, K. B., Glycerol Oxidation on Nickel Based Nanocatalysts in Alkaline Medium – Identification of the Reaction Products. *J. Electroanal. Chem.* **2013,** *703*, 56-62.

52. Rios, X.; Moriones, P.; Echeverría, J. C.; Luquin, A.; Laguna, M.; Garrido, J. J., Ethyl Group as Matrix Modifier and Inducer of Ordered Domains in Hybrid Xerogels Synthesised in Acidic Media using Ethyltriethoxysilane (ETEOS) and Tetraethoxysilane (TEOS) as Precursors. *Mater. Chem. Phys.* **2013,** *141*, 166-174.

53. Li, J.; Zhang, L.; Yang, P.; Cheng, X., Morphological Evolution of Co Phosphate and Its Electrochemical and Photocatalytic Performance. *CrystEngComm* **2018,** *20*, 6982-6988.

54. Omar, F. S.; Numan, A.; Duraisamy, N.; Bashir, S.; Ramesh, K.; Ramesh, S., Ultrahigh Capacitance of Amorphous Nickel Phosphate for Asymmetric Supercapacitor Applications. *RSC Adv.* **2016,** *6*, 76298-76306.

55. Frost, R. L.; Scholz, R.; López, A.; Xi, Y., A Vibrational Spectroscopic Study of the Phosphate Mineral Whiteite $CaMn^{++}Mg_2Al_2(PO_4)_4(OH)_2 \cdot 8(H_2O)$. *Spectrochim. Acta A* **2014,** *124*, 243-248.

56. Shu, Y.; Li, B.; Chen, J.; Xu, Q.; Pang, H.; Hu, X., Facile Synthesis of Ultrathin Nickel–Cobalt Phosphate 2D Nanosheets with Enhanced Electrocatalytic Activity for Glucose Oxidation. *ACS Appl. Mater. Interfaces* **2018,** *10*, 2360-2367.

57. Zhao, C.; Wang, S.; Zhu, Z.; Ju, P.; Zhao, C.; Qian, X., Roe-Shaped $Ni_3(PO_4)_2$/RGO/$Co_3(PO_4)_2$ (NRC) Nanocomposite Grown In Situ on Co Foam for Superior Supercapacitors. *J. Mater. Chem. A* **2017,** *5*, 18594-18602.

58. Bhanja, P.; Kim, Y.; Paul, B.; Lin, J.; Alshehri, S. M.; Ahamad, T.; Kaneti, Y. V.; Bhaumik, A.; Yamauchi, Y., Facile Synthesis of Nanoporous Transition Metal-Based Phosphates for Oxygen Evolution Reaction. *ChemCatChem* **2020,** *12*, 2091-2096.

59. Gond, R.; Singh, D. K.; Eswaramoorthy, M.; Barpanda, P., Sodium Cobalt Metaphosphate as an Efficient Oxygen Evolution Reaction Catalyst in Alkaline Solution. *Angew. Chem. Int. Ed.* **2019,** *58*, 8330-8335.

60. Zhao, D.; Shao, Q.; Zhang, Y.; Huang, X., N-Doped Carbon Shelled Bimetallic Phosphates for Efficient Electrochemical Overall Water Splitting. *Nanoscale* **2018,** *10*, 22787-22791.

61. Li, G.; Anderson, L.; Chen, Y.; Pan, M.; Abel Chuang, P.-Y., New Insights into Evaluating Catalyst Activity and Stability for Oxygen Evolution Reactions in Alkaline Media. *Sustain. Energy Fuels* **2018,** *2*, 237-251.

62. Jung, S.; McCrory, C. C. L.; Ferrer, I. M.; Peters, J. C.; Jaramillo, T. F., Benchmarking Nanoparticulate Metal Oxide Electrocatalysts for the Alkaline Water Oxidation Reaction. *J. Mater. Chem. A* **2016,** *4*, 3068-3076.

63. Sun, Y.; Gao, S.; Lei, F.; Liu, J.; Liang, L.; Xie, Y., Atomically-Thin Non-Layered Cobalt Oxide Porous Sheets for Highly Efficient Oxygen-Evolving Electrocatalysts. *Chem. Sci.* **2014,** *5*, 3976-3982.

64. Zeng, L.; Zhou, K.; Yang, L.; Du, G.; Liu, L.; Zhou, W., General Approach of in Situ Etching and Doping To Synthesize a Nickel-Doped M_xO_y (M = Co, Mn, Fe) Nanosheets Array on Nickel Foam as Large-Sized Electrodes for Overall Water Splitting. *ACS Appl. Energy Mater.* **2018,** *1*, 6279-6287.

65. Zhang, J.; Li, X.; Liu, Y.; Zeng, Z.; Cheng, X.; Wang, Y.; Tu, W.; Pan, M., Bi-Metallic Boride Electrocatalysts with Enhanced Activity for the Oxygen Evolution Reaction. *Nanoscale* **2018,** *10*, 11997-12002.

66. Wang, J.; Zeng, H. C., CoHPi Nanoflakes for Enhanced Oxygen Evolution Reaction. *ACS Appl. Mater. Interfaces* **2018,** *10*, 6288-6298.

67. Ray, C.; Lee, S. C.; Jin, B.; Kundu, A.; Park, J. H.; Jun, S. C., Stacked Porous Iron-Doped Nickel Cobalt Phosphide Nanoparticle: An Efficient and Stable Water Splitting Electrocatalyst. *ACS Sustain. Chem. Eng.* **2018,** *6*, 6146-6156.

68. Wan, K.; Luo, J.; Zhou, C.; Zhang, T.; Arbiol, J.; Lu, X.; Mao, B.-W.; Zhang, X.; Fransaer, J., Hierarchical Porous Ni_3S_4 with Enriched High-Valence Ni Sites as a Robust Electrocatalyst for Efficient Oxygen Evolution Reaction. *Adv. Funct. Mater.* **2019,** *29*, 1900315.

69. Sun, Y.; Gao, S.; Lei, F.; Xie, Y., Atomically-Thin Two-Dimensional Sheets for Understanding Active Sites in Catalysis. *Chem. Soc. Rev.* **2015,** *44*, 623-636.

70. Yeo, B. S.; Bell, A. T., Enhanced Activity of Gold-Supported Cobalt Oxide for the Electrochemical Evolution of Oxygen. *J. Am. Chem. Soc.* **2011,** *133*, 5587-5593.

71. Li, J.; Wei, G.; Zhu, Y.; Xi, Y.; Pan, X.; Ji, Y.; Zatovsky, I. V.; Han, W., Hierarchical NiCoP Nanocone Arrays Supported on Ni Foam as an Efficient and Stable Bifunctional Electrocatalyst for Overall Water Splitting. *J. Mater. Chem. A* **2017,** *5*, 14828-14837.

72. Xu, N.; Cao, G.; Chen, Z.; Kang, Q.; Dai, H.; Wang, P., Cobalt Nickel Boride as an Active Electrocatalyst for Water Splitting. *J. Mater. Chem. A* **2017,** *5*, 12379-12384.

73. Li, Y.; Zhao, C., Iron-Doped Nickel Phosphate as Synergistic Electrocatalyst for Water Oxidation. *Chem. Mater.* **2016,** *28*, 5659-5666.

74. Zhao, C.; Li, P.; Shao, D.; Zhang, R.; Wang, S.; Zhu, Z.; Zhao, C., Phytic Acid-Derived $Co_{2-x}Ni_xP_2O_7$-C/RGO and Its Superior OER Electrocatalytic Performance. *Int. J. Hydrog. Energy* **2019,** *44*, 844-852.

75. Zhan, Y.; Lu, M.; Yang, S.; Xu, C.; Liu, Z.; Lee, J. Y., Activity of Transition-Metal (Manganese, Iron, Cobalt, and Nickel) Phosphates for Oxygen Electrocatalysis in Alkaline Solution. *ChemCatChem* **2016,** *8*, 372-379.

TABLE OF CONTENT (TOC) DESCRIPTION

This work reports the self-stacking of nickel-cobalt phosphate nanoplates into porous 1D chain-like particles through template-assisted method for efficient oxygen evolution reaction.